POLITECNICO DI TORINO
Repository ISTITUZIONALE

Functional Nanocarbon Hybrids in Metal Oxide Nanocomposites for Photocatalysis

Terms of use:

Publisher copyright

(Article begins on next page)

19 February 2025

Article

Functional Nanocarbon Hybrids in Metal Oxide Nanocomposites for Photocatalysis

Paul P. Debes [1,2], Melanie Pagel [1,2], Simeon Muntean [1,2], Janis Hessling [3], Bernd M. Smarsly [1,2], Monika Schönhoff [3] and Teresa Gatti [1,2,4,*]

1   Center for Materials Research, Justus-Liebig University, Heinrich-Buff-Ring 17, 35392 Giessen, Germany; paul.debes@phys.chemie.uni-giessen.de (P.P.D.)
2   Institute of Physical Chemistry, Justus-Liebig University, Heinrich-Buff-Ring 17, 35392 Giessen, Germany
3   Institute of Physical Chemistry, University of Muenster, Corrensstrasse 28/30, 48149 Muenster, Germany; j_hess29@uni-muenster.de (J.H.); schoenho@uni-muenster.de (M.S.)
4   Department of Applied Science and Technology, Politecnico di Torino, C.so Duca degli Abruzzi 24, 10129 Torino, Italy
*   Correspondence: teresa.gatti@polito.it

Abstract: The textile industry is a major contributor to environmental pollution, primarily through the discharge of wastewater loaded with dyes and contaminants that disrupt natural ecosystems. This study aims to develop a hybrid material by functionalizing carbon nanodots (CNDs) with the donor-π-acceptor organic dye L1 via amide coupling. By chemically modifying the surface of CNDs, we can enhance their multifunctionality and tailor their molecular composition. This innovative approach seeks to replace expensive dyes with cost-effective CNDs synthesized from citric acid and ethylenediamine using a domestic microwave oven, potentially improving the stability of the resulting hybrid. Additionally, TiO_2 anatase particles were synthesized as a metal oxide platform and sensitized with both pristine materials and the CND-L1 hybrid. A range of physicochemical methods was employed to analyze the elemental, structural, and optical properties of these materials. In photocatalytic degradation tests of methyl orange, the sensitized catalysts demonstrated significantly improved efficiency compared to TiO_2 alone. While CNDs exhibited good stability and enhanced L1's stability, scavenger experiments revealed that holes and hydroxyl radicals play crucial roles in the degradation mechanism. This research underscores the promise of CND hybrids in advancing pollutant degradation technologies while reducing reliance on costly photocatalysts.

Keywords: carbon nanodots; photocatalysis; sensitization; dye degradation; reusability

1. Introduction

A significant contributor to environmental contamination is the discharge of wastewater from the textile industry, which is often loaded with dyes and other pollutants. This wastewater ultimately reaches natural systems, causing further damage to the environment [1]. The rise of fast fashion and overconsumption has led to a corresponding increase in the production of inexpensive textiles, which are often produced without adequate consideration of the waste they generate. The multitude of chemicals utilized in these processes has the potential to cause significant health and safety issues for humans and the environment [2]. Additionally, the primary route of release into the natural ecosystem occurs via aqueous media, resulting in rapid and continuous contamination of marine and ground water resources. Given that textile production is predominantly concentrated in

countries with inadequate infrastructure for waste management and regulatory oversight, the resulting pollution directly poses a considerable health risk to the local ecosystem and population [1,3]. In order to address this issue, a number of methods are currently being explored and have already been deployed with the objective of reducing the quantity of pollutants released. The majority of methods employed to reduce the concentration of harmful dyes in aqueous solutions are based on biological and physicochemical approaches. These approaches are highly effective in removing pollutants. However, the high sensitivity of biological systems to external conditions makes them difficult to apply in a versatile manner [4–6]. In the case of physicochemical approaches, the removal of pollutants is usually accompanied by the formation of secondary waste products, which only serve to distort the problem rather than solving the pollution issue [7,8].

Since the discovery of the properties of titanium dioxide (TiO_2) as a photocatalyst a few decades ago, research on photoinduced reactions has increased considerably [9]. In particular, photocatalysis offers a promising approach to the remediation of pollution, with a considerable number of photocatalytic systems being researched [10,11]. The products of these catalytically driven reactions are reactive oxygen species (ROS), such as $^{\bullet}OH$ and $^{\bullet}O^{2-}$. These can further react with organic, inorganic or pathogenic contaminants, including viruses, leading to oxidative decomposition of the pollutants [12]. When considering the energy cost, solar light provides a simple and sustainable energy source for the procedure. This, in combination with the complete degradation of the pollutants, without the formation of by-products, offers a highly promising alternative compared to commonly used wastewater treatment methods [13]. TiO_2 is one of the most extensively researched materials in the field of photocatalysis, given its high abundance, low toxicity and chemical stability. A significant drawback is its high band gap energy of approximately 3.0–3.2 eV, which only permits light absorption below a wavelength of 390 nm, thereby accessing approximately 5% of the solar energy spectrum [14–16]. To address this limitation, a plethora of modifications can be implemented to enhance the degradation rate. These include heteroatom doping, morphological modification, and post-synthetic surface modification [17,18]. Dye sensitization represents a process that has been the subject of extensive research with the objective of increasing the absorption of light by a material. Research in this field has been particularly focused on dye-sensitized solar cells (DSSCs), where the enhancement of solar light absorption represents one of the key objectives in the advancement of energy production technologies [19,20]. Beyond DSSCs, this method offers improvement for various approaches of photoinduced processes, including photocatalysis [21]. The dye-sensitization process has been observed to enhance photocatalytic activity in comparison to alternative methods, such as doping, thereby underscoring its potential as a viable approach in visible-light photocatalysis [22–24]. The efficiency of dye-sensitized catalysts in facilitating charge separation through rapid electron injection from the excited state of the dye to the conduction band of TiO_2 has led to their emergence. The prospect of utilizing a class of catalysts capable of functioning under visible light irradiation, in conjunction with the potential for the recovery and reuse of photosensitizers, renders this process both environmentally and economically viable. However, the synthesis and cost of structurally complex dye molecules present challenges that must be considered when exploring dye-sensitization strategies. It is crucial to optimize the utilization of these dyes in order to facilitate broader applications of this technique in a more accessible and cost-effective manner.

The term "carbon dots" (CDs) collectively refers to a group of nanoscale carbonaceous particles that have been the subject of scientific interest since their initial discovery in 2004 [25]. Based on the synthetic approach employed, CDs can be classified into subcategories, including carbon nanodots (CNDs), carbon quantum dots (CQDs), and graphene

quantum dots (GQDs). Classification according to the presence of sp^2-carbon, size, heteroatom content, or photoluminescent (PL) properties may be employed as a means of differentiating between the various types of CDs [26]. CNDs are amorphous carbonaceous particles, whereas CQDs contain a sp^2-hybridized carbon core. GQDs exhibit a layered structure and a composition analogous to that of graphene and graphite [27]. The bottom-up synthetic approach of CNDs, which employs simple organic molecules such as citric acid (CA), amino acids, and ethylene diamine (EDA), allows for significant variation in the surface functional group composition, rendering it a promising candidate for further modification [28–31]. In particular, the functionalization of CNDs with organic dye molecules has the potential to enhance their applications in hydrogen evolution and bio-imaging by extending their light-absorbing capabilities [32,33].

The objective of the present study is to synthesize a hybrid species by functionalizing CNDs derived from CA and EDA with an organic dye via amide coupling. The hybrid is then combined with TiO$_2$ particles for the purpose of assessing its photocatalytic performance in dye degradation reactions under light irradiation. Characterization is conducted using UV-Vis spectroscopy, X-ray photoelectron spectroscopy (XPS), X-ray diffraction (XRD), and scanning electron microscopy (SEM) to evaluate the optical properties, crystal phase, atomic composition, and size. In order to gain insight into the sensitization process, the characterization includes elemental analysis (EA) and thermogravimetric analysis (TGA). The catalytic degradation of methyl orange (MO) under UV irradiation can be monitored through absorbance measurements for the four catalysts comprising TiO$_2$, TiO$_2$-CND, TiO$_2$-dye, and TiO$_2$-hybrid. Finally, the degradation efficiency of the catalysts is evaluated, with special regard to determining catalytic activity relative to dye content, with the objective of minimizing the use of costly sensitizers. Moreover, reusability, and scavenger experiments are conducted to further examine the catalysts' stability and the varying involvement of reactive species. Scavengers are compounds that trap an oxidizing species or electron holes in order to diminish the respective participation in the degradation [34]. Commonly used scavengers include ethylenediaminetetraacetic acid (EDTA) and isopropyl alcohol (IPA). The use of scavengers to suppress the degradation of target molecules, such as MO, facilitates the identification of the most active ROS or charge carriers in the photocatalytic process. This technique offers valuable insight into the contribution and behavior of different reactive species in the overall degradation mechanism.

2. Results & Discussion

The synthesis of CNDs involved a microwave (MW)-assisted reaction between CA and EDA at a 1:1 ratio, followed by purification through filtration and size-exclusion chromatography [35]. To verify their presence and assess their properties, the synthesized CNDs were subjected to thorough characterization using atomic force microscopy (AFM), ultraviolet-visible (UV-Vis) absorbance, PL, and nuclear magnetic resonance (NMR) spectroscopy. The dimensions of the CNDs were characterized using AFM. As illustrated in Figure S1, the CNDs exhibit an average size of 2.0 ± 0.4 nm. In a previous study, the presence of CNDs featuring surface-exposed primary amine groups was reported [28]. These groups are capable of undergoing further functionalization via an amide coupling reaction. The synthesis and characterization of the donor-π-acceptor dye L1, which was synthesized for subsequent functionalization of the CNDs, is described herein (Figure 1). L1 is a commercially available dye that is utilized in the fabrication of DSSCs and in a multitude of applications within low-cost light-energy harvesting and conversion [36,37]. The CND-L1 hybrid underwent purification via filtration using a syringe filter and size exclusion gel chromatography.
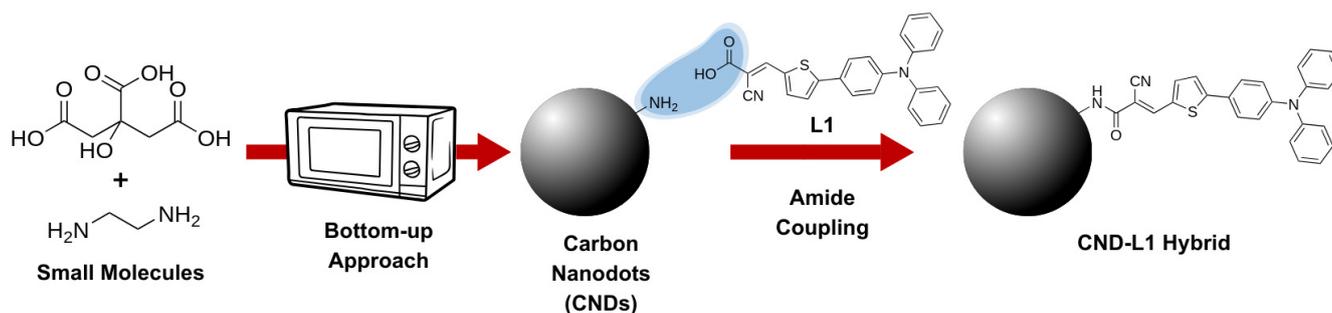
Figure 1. Schematic representation depicting the synthesis of CND from CA and EDA (1:1) via a MW-assisted reaction in water. This is followed by the amide coupling between the CND and the dye L1, which yields the CND-L1 hybrid.

To validate the successful functionalization of the CND with L1, diffusion-ordered spectroscopy (DOSY) NMR was employed. A comparable methodology was utilized by Prato and colleagues in 2018 to illustrate the covalent functionalization of CNDs [38]. Bare L1, pristine CND, a physical mixture of CND and L1, and the CND-L1 hybrid were subjected to 2D DOSY NMR as well as diffusion decay analysis. In all cases an integral over the chemical shift region from 8.9 to 6.4 ppm was evaluated, since in mixed and hybrid samples no separate L1 resonances could be identified. The results demonstrated a single diffusion/distribution profile for the L1, CND, and CND-L1 hybrid samples, indicating that the constituents of these samples are present in a mono-dispersed state. In contrast, the physical mixture of CND and L1 demonstrates two discrete diffusion distributions, indicating that the two moieties exhibit independent movement in the mixture (Figures S2–S5). In order to obtain more detailed quantitative data, the diffusion coefficients were derived from the diffusion echo decays (see Figure 2A) by applying the Stejskal-Tanner equation (see Supplementary Materials, Equation (S1)) [39]. Assuming a log-normal distribution of the diffusion coefficients (see Supplementary Materials, Equations (S2) and (S3)) resulted in the distributions in Figure 2B. The diffusion coefficient of pure L1 is depicted as a dotted red line at 1.94×10^{-10} m^2 s^{-1}, as it does not possess a size distribution, in contrast to the CND or the CND-L1 hybrid. The pristine CND sample exhibits the maximum value for the particle diffusion coefficient (D), with a value of 1.07×10^{-10} m^2 s^{-1}. The diffusion coefficient of the CND-L1 hybrid was found to be 33% lower than that of the pure CND, with a value of 0.72×10^{-10} m^2 s^{-1}. As the particle size increases, the diffusion coefficients decrease, which is consistent with the successful functionalization of the CND. In contrast, the physical mixture of CND with L1 exhibits two distinct peaks in the diffusion domain of the 2D spectrum (Figure S4), which can be viewed as separate peaks in the distribution of diffusion coefficients in Figure 2B. The fast component exhibits a diffusion coefficient similar to that of bare L1. Moreover, the diffusion coefficient of the CNDs in the mixture, represented by the shoulder with the lower diffusion coefficient, agrees to that of bare CND. This shows that the physical mixture consists of L1 and CND as separate species. In contrast, the sample with the hybrid lacks any component with a fast diffusion coefficient, indicating the absence of single L1 molecules, while the diffusion of the CND particles is slowed down, reflecting the increase of radius due to functionalization.
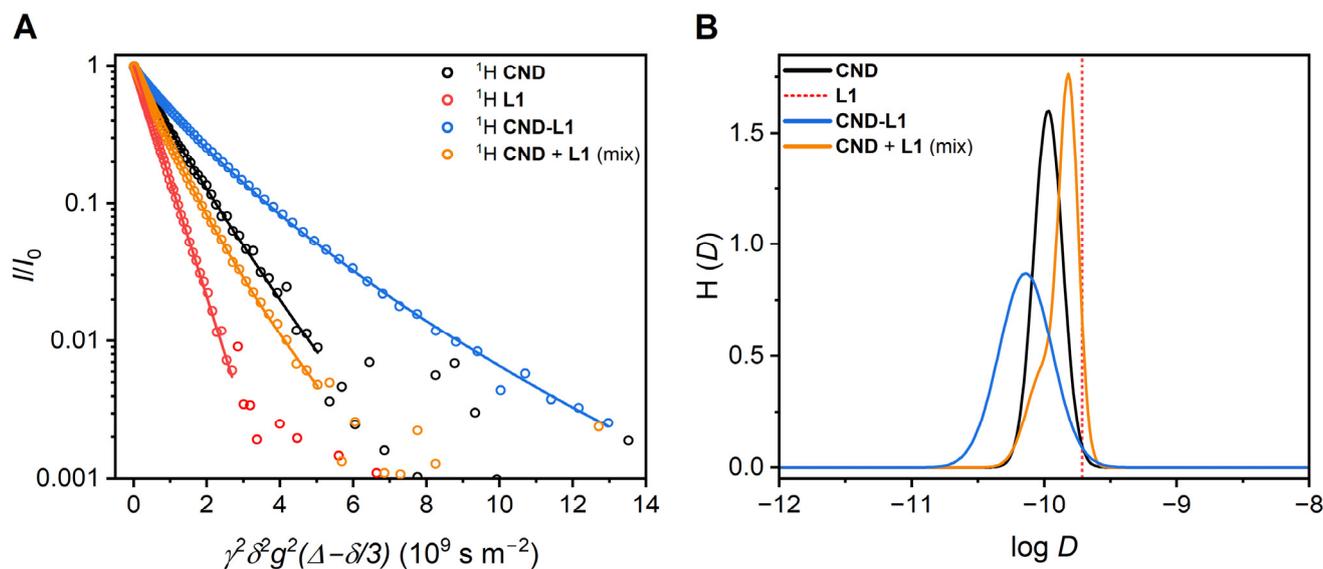
Figure 2. (**A**) The ^{1}H diffusion decay measurements, with shifts ranging from 8.9 ppm to 6.4 ppm, were conducted for CND, L1, as well as for a physical mixture of CND and L1 in a 10:1 weight ratio, and the CND-L1 hybrid. (**B**) The diffusion coefficients were analyzed using the method described by Lenoch et al. (2023) [40], which illustrates the diffusion coefficient distributions of CND, L1 (represented as a straight dotted line due to its lack of size distribution), the physical mixture of CND and L1 (10:1), and the CND-L1 hybrid.

In applying the Stokes–Einstein equation (see SI, Equation (S4)), the hydrodynamic diameter can be determined from the maximum diffusion coefficient. In this way the dimensions of the CND have been determined to be 1.9 nm, while CND-L1 exhibits a diameter of 2.8 nm (Table 1). The dimensions of the CND are consistent with the findings of the AFM analysis.

Table 1. Maximum of the diffusion coefficient distribution obtained from fitting of echo decays, along with the hydrodynamic diameter calculated using the Stokes–Einstein equation.

Sample	$D/m^2\ s^{-1}$	Hydrodynamic Diameter/nm
CND	1.07×10^{-10}	1.90
L1	1.94×10^{-10}	1.00
CND + L1 (physical mix) †	0.98×10^{-10}	2.00
	1.53×10^{-10}	1.30
CND-L1	0.72×10^{-10}	2.80

† The physical mixture corresponds to a weight ratio of 10:1 of CND to L1.

The UV-Vis and PL spectra of pure CND, L1, and the CND-L1 hybrid are presented in Figure 3. CND displays an absorption maximum at 357 nm, accompanied by a corresponding emission maximum at 443 nm. L1 displays absorption at both 302 nm and 412 nm, with the latter being the more prominent of the two. An emission maximum was observed at 550 nm ($\lambda_{Ex,\ L1}$ = 412 nm). A comparison of the spectra of pure CND and L1 with those of CND-L1 reveals the presence of a combination of both initial materials, with absorption at 302 nm, 357 nm, and 454 nm. However, while the absorption originating from the CND molecule is identical, the absorption originating from L1 at 412 nm exhibits a red shift, with a maximum at 454 nm. No notable shift in the emission spectra was observed for the CND-L1 hybrid.
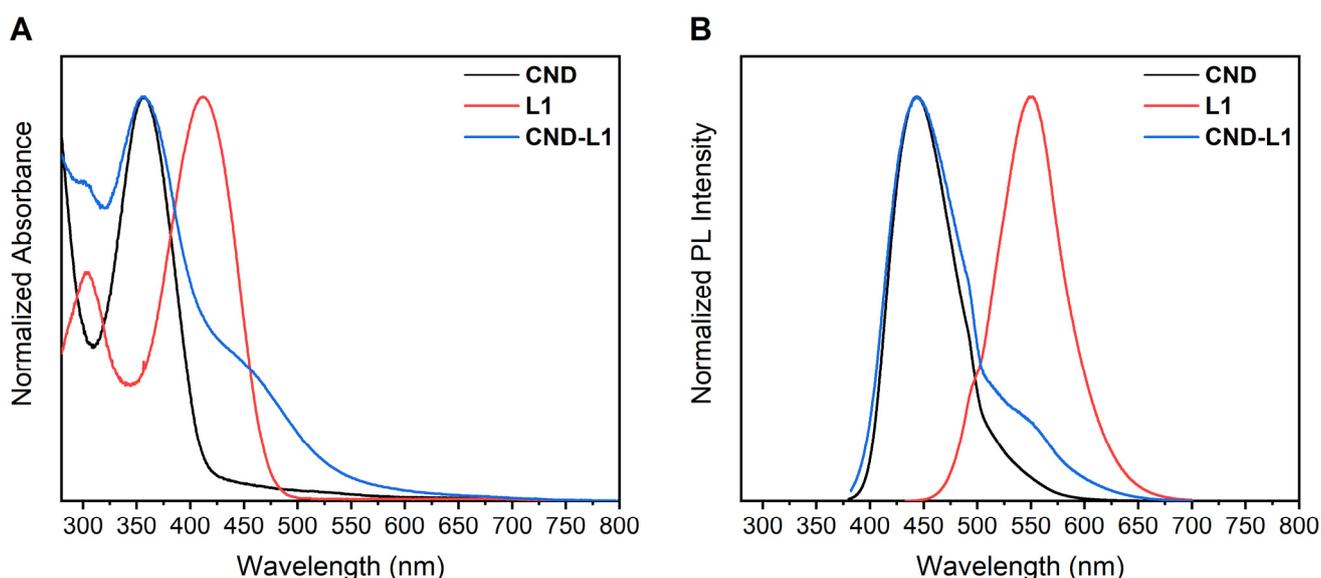
A

B

Figure 3. Normalized (**A**) absorbance and (**B**) PL of CND (black lines), L1 dye (red lines), and CND-L1 hybrid (blue lines).

The photoluminescence quantum yield (PLQY) of CND was found to be 39.0%, that of L1 6.8%, and of the CND-L1 hybrid 9.6% (Figure S6), as determined by the relative method with quinine sulfate as the reference. The functionalization of CND resulted in a notable decrease in PLQY, indicating that the surface amines of CND may have undergone functionalization, potentially leading to a non-radiative de-excitation pathway [41,42]. This is because surface states are a significant source of PL in CNDs [29]. Furthermore, a through-space mechanism, such as Förster resonance energy transfer (FRET) or electron transfer, is a viable option, given the close proximity of the units [43–46]. FRET is based on a dipole-dipole interaction, where the resonance between the donor's emission and the acceptor's absorbance and the relative orientation of their transition dipole moments are crucial [47]. In contrast, electron transfer necessitates a substantial overlap between the donor and acceptor orbitals, a prerequisite that is plausible. As demonstrated in Figure 3, the CND emission strongly overlaps with the dyes absorbance, rendering a FRET from CND to the L1 dye feasible [48,49]. Both FRET and electron transfer generally result in a reduced PLQY. This outcome indicates the potential for both FRET and the process of charge transfer to influence the overall efficiency of quenching. It is noteworthy that the efficiency of charge transfer is significantly dependent on the concentration of acceptor molecules in the system. The absence of a well-defined structural configuration in the synthesized hybrid and the imprecise determination of the number of dye molecules residing on the surface of a single CND hinders the precise quantification of the respective contributions of charge and electron transfer processes [45]. The data presented in Table 2 provides a comprehensive overview of the absorption and emission characteristics, as well as the PLQY, and absorption coefficient, of the pristine and functionalized samples (Figures S6 and S7). In addition, the excitation–emission maps and the excitation spectra are in agreement with the previously mentioned results (Figures S8 and S9).

Table 2. UV-Vis absorption maxima (λ_{Abs}), PL maxima (λ_{Em}), Stokes shift, PLQY, and absorption coefficient (ε at 412 nm) of the CND-L1 hybrid compared to pristine CND, and L1.

Sample	λ_{Abs}/nm	λ_{Em}/nm	Stokes Shift/nm	PLQY/%	ε_{412nm}/L g^{-1} cm^{-1}
CND	357	443	86	39.0	0.79
L1	412	550	138	6.8	92.7
CND-L1	357	443	86	9.6	3.29

TGA reveals a significant weight loss for CND, L1, and the CND-L1 hybrid between 100 °C and 300 °C, as illustrated in Figure S10. Both CND and L1 exhibit decomposition within a similar temperature range. Notably, the TGA profiles of the CND-L1 hybrid demonstrate a greater mass loss compared to that of pure CND, suggesting the occurrence of functionalization. The residues at 900 °C during the TGA measurement would correspond to approximately a 50% mass fraction of dye L1 in the CND-L1 hybrid. However, the XPS and EA measurements do not indicate this 50% ratio; instead, they show a strong similarity to pure CND, suggesting a significantly lower proportion of dye in the hybrid (Figure S11). Nonetheless, the concurrent degradation of both components and the considerable changes in the morphology of the CND limit the ability to accurately quantify the extent of functionalization. For this reason, a deconvolution of the absorption spectrum of the CND-L1 hybrid was performed, with the aim of separating it into its two components, L1, and CND. This was achieved by utilizing four Gaussian functions (Figure S12). By employing the absorbance of the dye L1 at 454 nm, derived from the deconvolution contribution, and assuming that the experimental absorption coefficient of the pure dye L1 at 412 nm can be applied, we can calculate the corresponding concentration using Beer-Lambert's law. The concentration of the CND-L1 hybrid is known, consequently from the absorption spectrum we can estimate the weight percentage of L1 dye to be 2.2%. In our previous study, we demonstrated that the CND under consideration could be functionalized up to 80 µmol g^{-1} via an amide coupling, with the 2.2% calculated here corresponding to approximately 50 µmol g^{-1} [28]. The larger size of the L1 dye in comparison to the moiety utilized in our previous study led to a slight reduction in the degree of functionalization. We therefore assume the 2.2% of L1 dye on the CND-L1 with a reasonable degree of approximation.

TiO$_2$ particles were synthesized at a calcination temperature of 350 °C with a heating ramp of 2 °C min^{-1} [50]. The selection of a lower calcination temperature was intended to produce TiO$_2$ particles with an increased surface area, which may result in a higher density of surface hydroxyl groups. It is anticipated that this enhancement will facilitate greater degrees of sensitization and improved photocatalytic activity [18]. A nitrogen physisorption (77 K) isotherm was used to determine the surface area of the TiO$_2$ particles using the BET approach, resulting in a value of 82 m^2 g^{-1} (Figure S13). In the low-pressure regime of the isotherm, the presence of microporosity is negligible, while the majority of the pore volume is comprised of mesopores in the form of interstitial particle space, with a mode diameter of 12 nm. The SEM images indicate a particle size of 31 ± 5 nm, in addition to the presence of aggregated particles in an aqueous solution, with an average diameter of 685 ± 160 nm, as determined by dynamic light scattering (DLS) measurements (Figure S14). The XRD measurements indicate that the synthesized TiO$_2$ particles consist entirely of anatase, as only reflections corresponding to the anatase phase are observed (Figure S15). In the following step, the synthesized TiO$_2$ particles were sensitized with CNDs, L1 dye, and CND-L1 hybrid in acetonitrile. The resulting mixture was then subjected to centrifugation, and the particles were washed multiple times with water through sonication and centrifugation. This process yielded three distinct sensitized photocatalysts, namely: TiO$_2$-CND, TiO$_2$-L1, and TiO$_2$-CND-L1 (Figure 4).
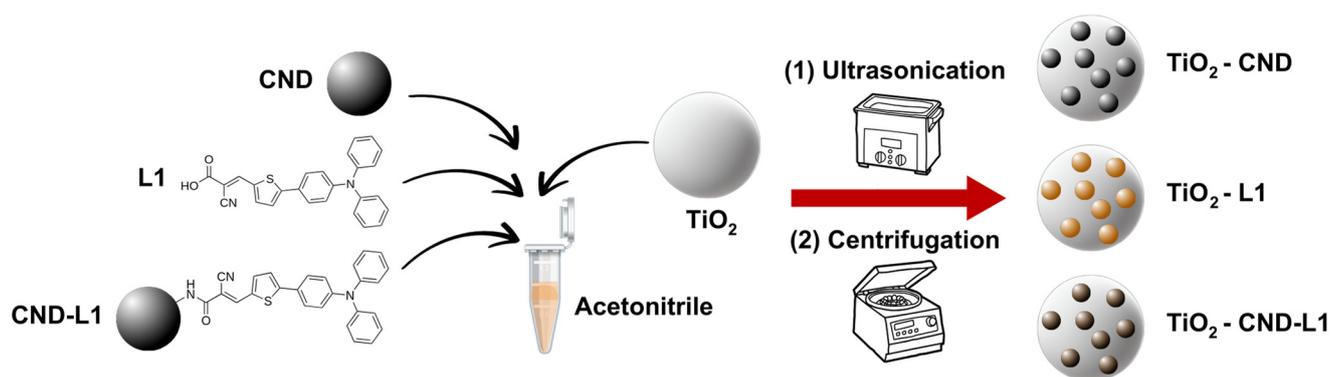
Figure 4. Schematics of the TiO$_2$ nanoparticles sensitization process with CNDs, L1 dye, and a CND-L1 hybrid. After this initial step, the mixture was treated with ultrasonication followed by centrifugation. The particles were subsequently washed several times with water using a combination of sonication and centrifugation. This procedure resulted in the formation of three unique sensitized photocatalysts: TiO$_2$-CND, TiO$_2$-L1, and TiO$_2$-CND-L1.

A visible color change from white to yellow, red, and brown was observed for TiO$_2$-CND, TiO$_2$-L1, and TiO$_2$-CND-L1, respectively. This prompted us to perform diffuse reflectance spectroscopy on both the TiO$_2$ and sensitized catalysts (Figure 5). The spectra of the sensitized samples unambiguously demonstrate that the absorbance range of pristine TiO$_2$ is extended in the region between 400 nm and 600 nm, which is indicative of a successful sensitization process. The indirect band gap of TiO$_2$ anatase particles was determined to be 3.19 eV through the conversion of diffuse reflectance data to the Kubelka–Munk function [51] and the subsequent application of Tauc plot [52] analysis (Figure S16).
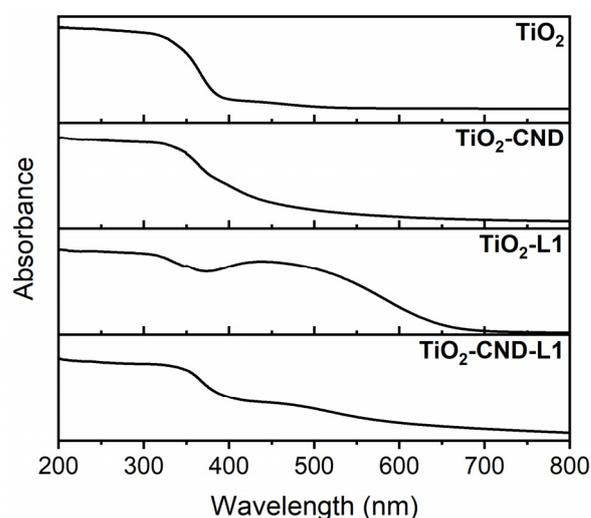

Figure 5. Diffuse reflectance spectra of TiO$_2$ nanoparticles compared to the three sensitized TiO$_2$ samples: TiO$_2$-CND, TiO$_2$-L1, and TiO$_2$-CND-L1.

Furthermore, XPS measurements were conducted, the results of which are presented in Figure S17. As previously demonstrated in Figure S11, the XPS analysis of the pure L1 dye and CND-L1 hybrid exhibited a negligible sulfur content, rendering its detection on the nanocomposite challenging. XPS is a highly surface-sensitive method that does not consider the entire particle, but rather a limited area on the surface. Considering the total amount of 12 mg sensitizer added to the 500 mg TiO$_2$, the theoretically calculated mass fraction of all three sensitizers on TiO$_2$ is 2.34%, but it should be noted that the mass fraction might differ due to the washing steps. Accordingly, the resulting mass fractions were determined by TGA measurements and are presented in Figure S18. The

actual loading of CND, L1, and CND-L1 on the TiO$_2$ particles was determined at 900 °C, resulting in a weight loss of 0.73%, 1.27%, and 2.70%, respectively. It is assumed that all organic matter on the catalyst will be decomposed at 900 °C. The observed increase in weight at temperatures above 500 °C is thought to result from the possible phase transition from amorphous powder to anatase phase [53]. The different adsorption capabilities of the sensitizers may be attributed to interactions between the TiO$_2$ surface and the surface moieties of CND, L1, and CND-L1. The CND exhibits a plethora of oxygen- and nitrogen-based functional surface groups, including carboxylic acids, which are capable of coordinating with surface Ti in a monodentate or bidentate manner [54]. The L1 dye exhibits hydrophobic characteristics due to its apolar structure, which results in reduced absorbability onto TiO$_2$. In the hybrid, the accessible amine groups are functionalized with dye molecules, whereby the number of carboxylic acid moieties remains unaltered and can interact with TiO$_2$. Given that the preparation of the catalysts entails washing steps with water, the resulting catalyst loading can be explained by the fact that the CND will be washed off the most. The L1 dye will likely adsorb less due to a low number of moieties for coordination. By combining the hydrophobic properties of the L1 dye with the large number of coordinating functional groups of CND, the CND-L1 hybrid enables the highest amount of adsorbed species. A rapid decline in mass of 0.3% can be observed at about 580 °C in the TGA measurement of the TiO$_2$-CND-L1 (Figure S18). This indicates that the mass fraction of the CND-L1 hybrid on the TiO$_2$ nanoparticles is approximately 2.4%. Given potential deviations, this value is reasonable and aligns with the maximum theoretical value of 2.34%.

In this study, pure TiO$_2$, CND-, L1-, and CND-L1-sensitized TiO$_2$ catalysts are employed to investigate the impact of sensitization on the catalytic performance. The photocatalytic degradation process was conducted at a temperature of 22.5 °C. 10 mg of the catalyst were added to 10 mL of an aqueous MO solution (50 μM), and the mixture was stirred for 30 min in the absence of light. The pH of the MO solution was 6.5. In order to perform the catalysis, a beaker with continuous cooling at 22.5 °C and a 395 nm UV LED (Figure S19) has been employed. Each catalysis cycle was conducted for a period of 50 min, with 250 μL aliquots being sampled at 10-min intervals. The extent of the degradation process was determined by measuring the UV-Vis transmission of the solution of degraded MO, which exhibited a maximum absorbance at 464 nm. In order to quantify the degradation activity, the degradation efficiency and first-order kinetics were calculated using the following Equations (1) and (2), respectively.

$$\ln\left(\frac{A_0}{A_t}\right) = kt \tag{1}$$

$$\text{degradation efficiency}(\%) = \left(\frac{A_0 - A_t}{A_0}\right) \times 100 \tag{2}$$

In this case, A_0 represents the initial absorbance following adsorption equilibrium, k is the rate constant, t is time, and A_t is the absorbance at a given time t. Figure 6A–C illustrates the catalytic results in terms of normalized absorbance, first-order kinetics, and degradation efficiency. Moreover, the same catalysis procedure was conducted in the absence of irradiation to eliminate any significant effects of MO adsorption onto the catalyst's surface. This was done to exclude any non-irradiation-based degradation that could distort the results (Figure 6D). All sensitized TiO$_2$ catalysts exhibited a higher rate constant than the unfunctionalized TiO$_2$ nanoparticles. The rate constant of TiO$_2$-L1 is approximately five times higher than that of TiO$_2$-CND-L1. In comparison to TiO$_2$-CND,

however, the rate constant could be increased by 73% for the TiO$_2$-CND-L1 catalysts with dye functionalization (Table 3).
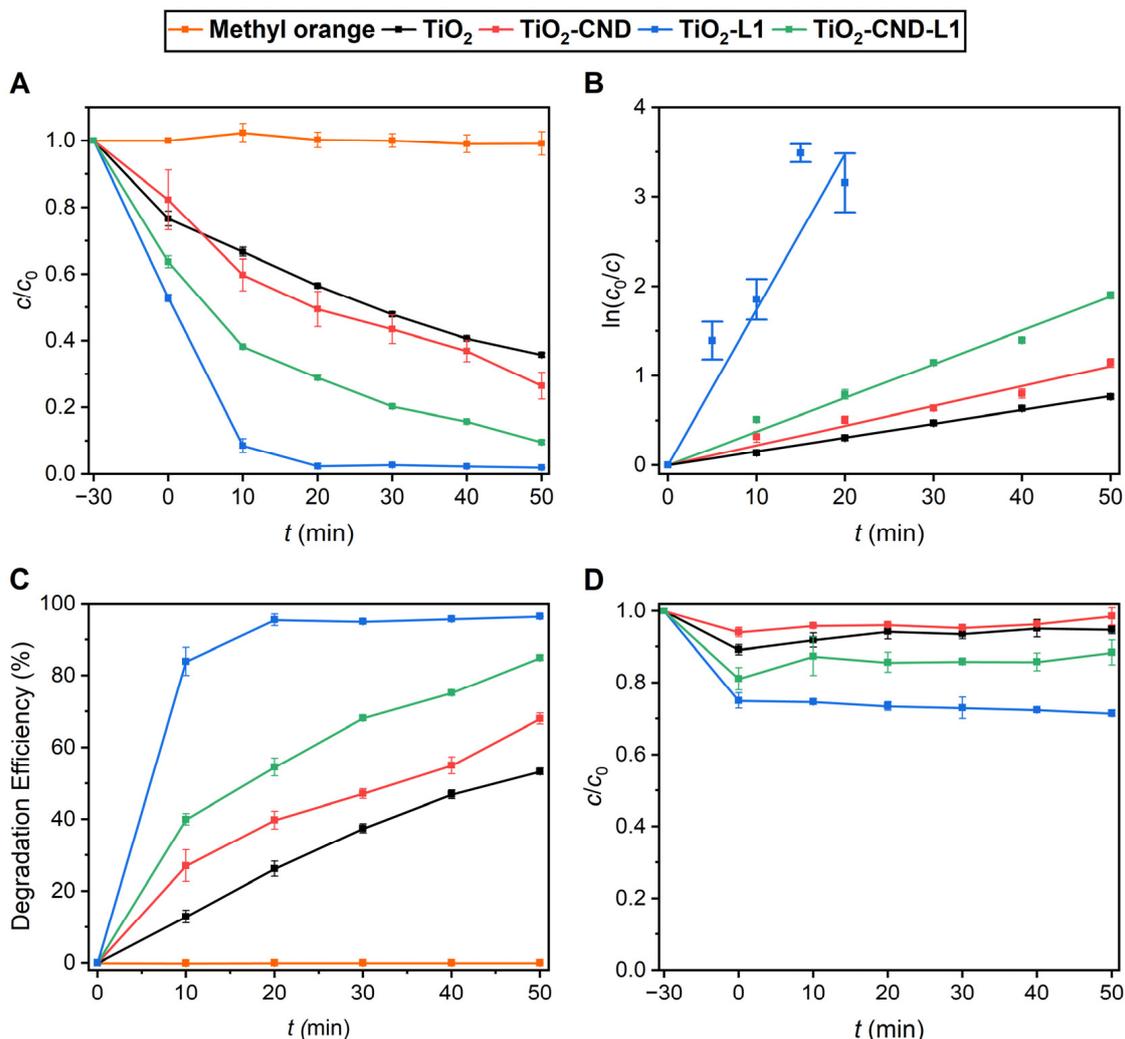

Figure 6. The results of the catalytic degradation are presented in three ways: (**A**) normalized absorbance measurements, (**B**) first-order kinetics analysis, and (**C**) degradation efficiency. These results demonstrate that all sensitized catalysts exhibit superior performance compared to bare TiO$_2$ and catalyst-free photolysis of MO. In the absence of irradiation, no significant degradation was observed (**D**), indicating that any potential adsorption or degradation occurring without irradiation is effectively negligible.

Table 3. First order kinetics rate constants *k* of the respective catalysts.

Sample	k/s^{-1}
TiO$_2$	0.16
TiO$_2$-CND	0.22
TiO$_2$-L1	1.74
TiO$_2$-CND-L1	0.38

In comparison to the photolysis of MO, a notable degree of degradation was observed for all TiO$_2$ materials. With regard to the composite catalysts, all three were found to enhance the overall catalytic performance. The pure TiO$_2$ underwent degradation of up to 50% of MO under UV irradiation, as a consequence of exciton formation. These excitons contribute to the degradation of MO either directly or indirectly through the production

of ROS, which further promote the decomposition process [55]. Among the composite materials, TiO_2-CND exhibited the lowest degradation efficiency, with a rate of 57%. The TiO_2-CND-L1 composite demonstrated up to 83% degradation over a 50-min irradiation period, whereas TiO_2-L1 exhibited complete degradation after 20 min. The elevated degradation rate observed in the composite materials relative to the pure TiO_2 can be attributed to two factors: firstly, the enhanced capability and range of light absorption. Secondly, the effective prevention of exciton recombination is achieved through the improved facilitation of excitons reaching the surface to react with the medium. The loading of the dye L1 for the catalysts, TiO_2-L1, and TiO_2-CND-L1, was calculated based on the amount of sensitizer present on the TiO_2 component via TGA (Figure S18). A total of 2.4% of the hybrid CND-L1 was identified on the surface of TiO_2-CND-L1. Based on the deconvolution of the UV-Vis spectrum of CND-L1 (Figure S12), it was determined that 2.2% of the hybrid can be attributed to the L1 dye. Consequently, the amount of L1 dye present in 10 mg of the TiO_2-CND-L1 catalyst has been determined to be 0.00538 mg. In contrast, the TiO_2-L1 catalyst contains 0.127 mg of the L1 dye in 10 mg of catalyst. This corresponds to a 24-fold increase in the amount of L1 dye present on the TiO_2-L1 catalyst surface. The functionalization of CND increases the ability to adsorb in combination with the dye, which contributes to efficient light absorption and electron transfer. The CND-L1 hybrid indicates a significant improvement in catalytic degradation depending on the amount of dye on the catalyst. In order to investigate the reusability of the catalysts, a reaction mixture consisting of 10 mg of the respective catalyst in the corresponding volume (1 mL MO solution per 1 mg catalyst) was irradiated for 50 min. The degradation efficiency of each catalyst is represented by gray bars following each catalytic cycle in Figure 7. The red bars additionally indicate the amount of catalyst that could be recovered for subsequent runs following the completion of each catalytic cycle. The values presented refer to the quantities weighted prior to the initiation of the first cycle.

The results of the TiO_2 measurements (Figure 7A) indicate an increase in the degradation efficiency of the catalyst, rising from an average degradation efficiency of 57.9% in the first cycle to 80.2% in the third cycle. This can be attributed to a post-synthesis aging process of the utilized TiO_2 particles. Some photocatalysts are known to require a period of use to reach their maximum efficiency due to changes in their structure [56]. Furthermore, we employed ultrasonication between each catalytic cycle, which has the potential to enhance the efficiency. In contrast, the other three modified catalysts, TiO_2-CND, TiO_2-CND-L1, and TiO_2-L1, exhibited a reversed trend, demonstrating a decline in efficiency during catalysis. The TiO_2-CND (Figure 7B) catalyst exhibited the lowest increase in degradation efficiency, while demonstrating the highest stability among the sensitized catalysts. In the initial cycle, TiO_2-CND achieved an efficiency of 73.5%, which decreased by 5.9% to 67.6% by the third cycle. The TiO_2-L1 catalyst (Figure 7C) demonstrated the highest degradation efficiency of 94.9% in the initial cycle, which subsequently decreased by 8.7% to 86.2% by the third cycle. In comparison, the TiO_2-CND-L1 catalyst (Figure 7D) exhibited a similarly high initial efficiency of 94.4%. However, this efficiency declined significantly, reaching 73.3% in the third cycle, which represents a 21.1% decrease. This observation indicates that, despite the TiO_2-CND-L1 catalyst having 24 times less dye on its surface, it maintains a comparable high efficiency to the TiO_2-L1 catalyst during the first cycle.
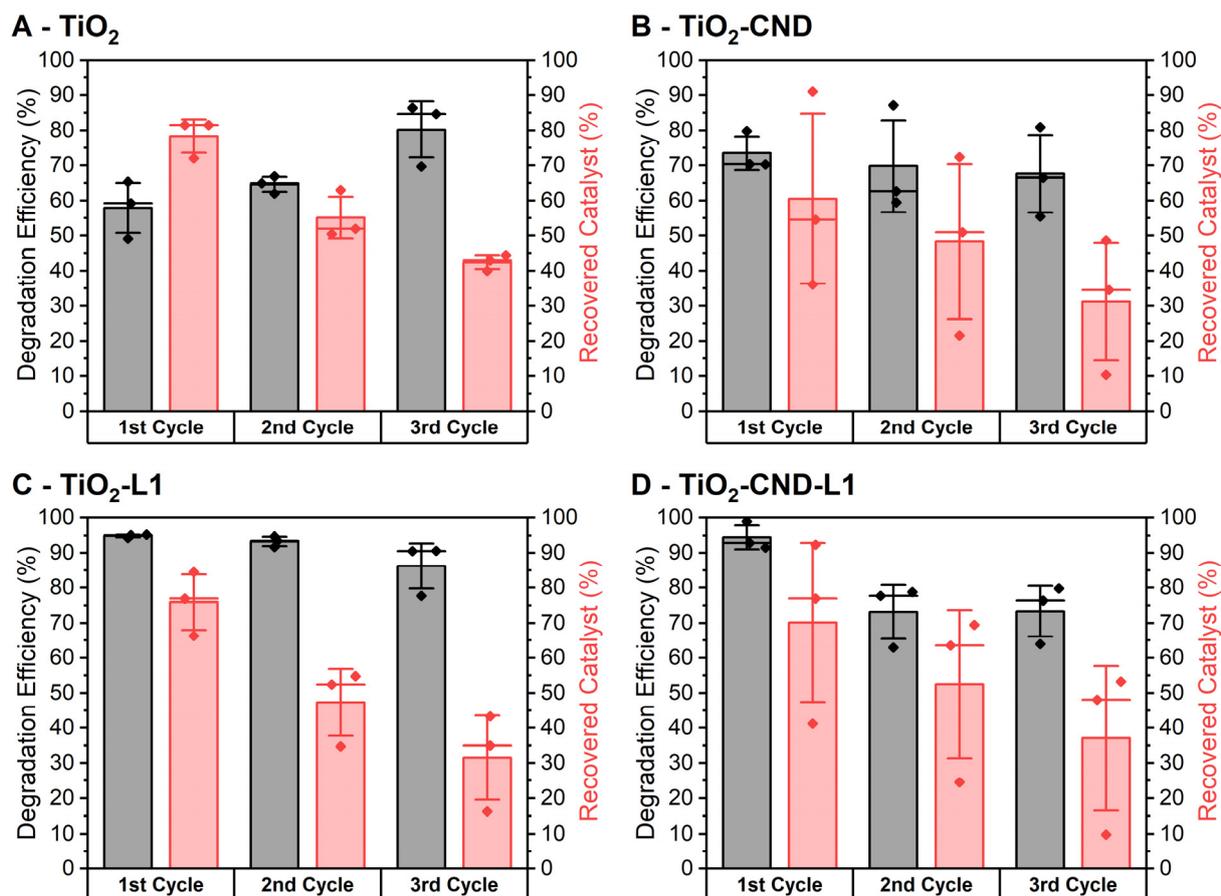
Figure 7. Degradation efficiency of the different catalysts (depicted in grey) and fraction of recovered catalyst after each cycle (depicted in red).

As illustrated in Figure 7C, the L1 dye does not demonstrate permanent photostability on the TiO_2 surface. It appears that the L1 dye was primarily degraded in the TiO_2-CND-L1 catalyst, as the efficiency in the second cycle decreased to 73.1%, which is comparable to the efficiency of the TiO_2-CND catalyst. This suggests that the CND was the sole active component in the TiO_2-CND-L1 catalyst from the second cycle onwards, while the L1 dye appears to have lost its activity. The markedly lower concentration of L1 dye in the TiO_2-CND-L1 catalyst compared to the TiO_2-L1 catalyst results in a more rapid depletion of the dye during photocatalytic activity. It can be concluded that covalent binding with CNDs does not result in a notable enhancement in the activity of the L1 dye. However, the dye appears to exhibit enhanced stability when bound to the CND.

In order to facilitate a more accurate comparison of the stability of the L1 dye within the TiO_2-L1 catalyst with that of the TiO_2-CND-L1 catalyst, we calculated the turnover number (TON). The TON is a metric for comparing the efficiency of different catalysts. It indicates the number of molecules of a reactant converted per active catalyst center until the catalyst is inactive. In this analysis, we assume that the L1 dye is the active center in the respective catalysts. In this context, a higher TON indicates that the L1 dye on the respective catalyst is more effective and can decompose a greater quantity of MO, thereby demonstrating superior catalytic conversion. In the case of the TiO_2-CND-L1 catalyst, it was assumed that the L1 dye would remain active only during the first cycle. Consequently, the amount of MO degraded during this first cycle was used as the basis for calculation. In the case of the TiO_2-L1 catalyst, the amount of MO degraded was taken from the total of three cycles. It is noteworthy that the L1 dye in the TiO_2-L1 catalyst retains partial activity following three cycles. The TON for the TiO_2-L1 catalyst was found

to be 1.57, while the TiO$_2$-CND-L1 catalyst exhibited a TON of 16.8 (see SI for details). Consequently, the TON for the TiO$_2$-CND-L1 catalyst is 10.7 times greater than that of the TiO$_2$-L1 catalyst (Figure 8). This suggests that, in order to achieve the same level of conversion as the TiO$_2$-CND-L1 catalyst, the L1 dye on the TiO$_2$-L1 catalyst would need to decompose 10.7 times more MO than it has done so far. In light of the observed decline in the efficiency of the TiO$_2$-L1 catalyst by 8.7% following three cycles and the fact that only 32% of the catalyst amount could be recovered after these three cycles, this result appears implausible. These findings indicate that the TiO$_2$-L1 catalyst exhibits notable limitations in sustainability when compared to its CND-modified counterpart. It is important to note that the presented catalysts herein are not run through an optimization process of the conditions influencing the catalytic performance yet, namely dye-concentration, mass of catalyst, pH value, temperature, wavelength, and radiant flux. This would require an in depth study to figure out the optimal catalytic efficiencies of each catalyst.
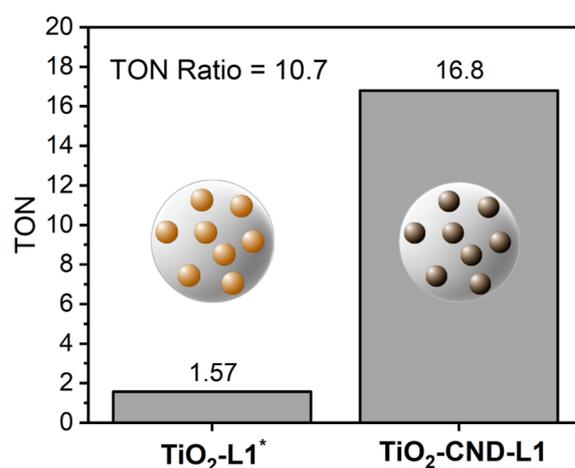

Figure 8. A comparison of the TON of the TiO$_2$-CND-L1 catalyst with that of the TiO$_2$-L1 catalyst, with relation to the quantity of L1 dye present on each catalyst. * The L1 dye in the TiO$_2$-L1 catalyst exhibits residual activity following three cycles.

In order to identify the reactive species involved in the degradation process of MO, a variety of scavenger reagents were employed. Scavengers are capable of trapping specific radicals that may form during the reaction. Consequently, a reduction in the degradation efficiency resulting from the presence of one of the scavenger compounds can be employed to evaluate the impact of the corresponding radical on the degradation mechanism. Specifically, *p*-benzoquinone (*p*-BQ) was employed as a scavenger for superoxide radicals ($^{\bullet}O^{2-}$), IPA was used to scavenge hydroxyl radicals ($^{\bullet}OH$), and EDTA was applied to capture holes (h$^+$).

p-BQ was observed to react with TiO$_2$ and the reaction mixture turned black (Figure S20), even in the absence of an MO solution. The change in color resulted in an inability to measure the UV-Vis absorbance of the MO. Accordingly, an alternative trapping agent for $^{\bullet}O^{2-}$ was selected. Mondol et al. conducted the scavenger experiment with ascorbic acid (AA) to investigate the presence of $^{\bullet}O^{2-}$ species [57].

The results indicate that the addition of EDTA significantly reduces the degradation efficiency of all catalysts (Figure 9). The presence of EDTA resulted in a notable decline in the degradation efficiency of the TiO$_2$ catalyst, with a reduction of the degradation efficiency of 53.6%. This was followed by the most pronounced decrease in the TiO$_2$-CND catalyst, with a reduction of 89.4%. The TiO$_2$-CND-L1 catalyst exhibited a moderate decline of 78.3%, while the TiO$_2$-L1 catalyst demonstrated the least significant reduction, of 47.7%. The role of the holes formed in the mechanism is of significant weight in each of the reactions. CNDs are capable of preventing the electron–hole recombination, which

increases the amount of electrons and holes available for catalysis, a phenomenon that can be observed in this experiment [58]. The addition of IPA resulted in a 23.3% reduction in the efficiency of the process for TiO_2, 23.4% for TiO_2-CND, 13.4% for TiO_2-CND-L1, and 15.0% for TiO_2-L1. Additionally, $^\bullet OH$ radicals are present in the MO degradation reaction with each catalyst, though they exert less influence on the subsequent reaction than h^+. In contrast to the observed decrease in degradation efficiency for the other catalysts, the addition of AA resulted in an increase of the degradation efficiency for all four catalysts. For TiO_2, the observed increase was 69.5%, while for TiO_2-CND, it was 32.0%. The remaining two catalysts had already nearly completely degraded the MO in the absence of scavenger molecules. However, the reference efficiencies were determined at a pH value above 4.4 at a wavelength of 464 nm, while the degradation efficiency with AA was calculated using the results of the UV-Vis measurement at 517 nm at pH 3.0. To eliminate the possibility that the acidic environment is responsible for the improvement in the reaction, reference measurements were performed without ascorbic acid, but at a pH value of 3.0. To prevent the introduction of other molecules into the solution that could act as scavengers, the solution was acidified with dilute HCl (Figure S21). A comparison with the aforementioned reference values also demonstrates that the reaction exhibits enhanced degradation efficiencies when AA is present in the reaction mixture. It has been demonstrated that AA can form a complex with TiO_2, which serves to mediate the formation of $^\bullet O^{2-}$. This enhances the photocatalytic decomposition of MO under UV light [59].
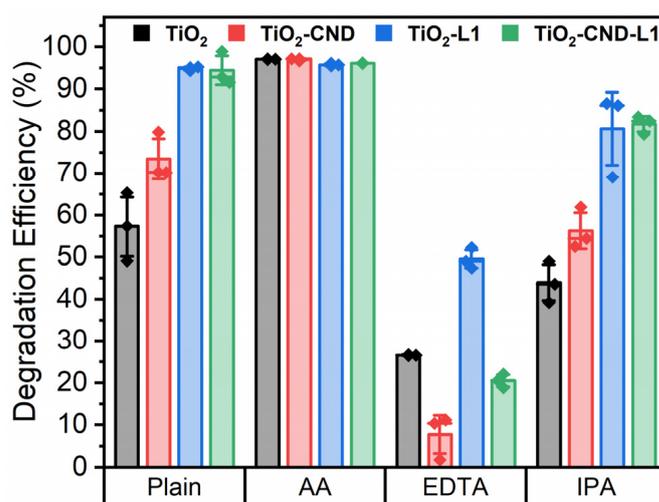

Figure 9. Effects of different radical scavengers on the MO degradation efficiency of the respective catalysts. Plain = no scavenger added; AA = ascorbic acid; EDTA = ethylenediaminetetraacetic acid; IPA = isopropyl alcohol.

The application of EDTA demonstrates the most significant scavenging effect, indicating that the predominant occurrence is the formation of holes in the mechanism. In general, heterojunction photocatalysts are designed to create junctions between the different materials. The implementation of this approach offers several advantages, including improved charge separation, enhanced catalytic activity, and broader light absorption [55]. Given that the energy levels of the various materials typically differ from one another, a resulting band offset is created at the interface. Following irradiation with light in both materials, electron–hole pairs are generated. Due to the band offset, electrons migrate from the conduction band (CB) of one material to the CB of the other material, while holes migrate in the opposite direction. This separation prevents recombination, thereby increasing the availability of electrons and holes for photocatalytic reactions [55].

In the absence of a scavenger or available trap states, the recombination of the electron and the hole is prevented. In response, the holes can act as powerful oxidants directly or indirectly, while the electron acts as a reductant [60]. The holes may also undergo further reactions with adsorbed water, hydroxides, and surface titanol groups, resulting in the formation of hydroxyl radical species. These species have the potential to promote the mineralization of MO. The presence of IPA was also found to result in the generation of hydroxyl radicals. It can thus be concluded that the main active species from the presented catalysts for MO degradation are holes, h^+, and hydroxyl radicals.

The degradation mechanism of MO is dependent on several parameters, including dye concentration, catalyst mass, wavelength, radiant flux, and the addition of oxidants or the presence of natural substances such as inorganic ions. A comprehensive analysis, including the detection and quantification of the various photoproducts, is essential for a detailed understanding of the degradation process [61]. Given the unconfirmed structural and energetic attributes of the CNDs, a comprehensive examination of the electron transfer and hole generation processes within the developed heterojunctions is not within the scope of this study.

3. Conclusions

In this study, MW-assisted synthesized CNDs derived from CA and EDA were employed to develop a novel hybrid material through amide coupling with the dye L1, which is recognized for its application in DSSCs. The optical characteristics of this hybrid were meticulously characterized using UV-Vis and PL spectroscopy, while its compositional analysis was conducted via XPS, EA, and TGA. The formation of covalent bonds between the CND and L1, along with the dimensions of the hybrid, was confirmed through DOSY NMR.

Subsequently, TiO_2 particles were synthesized and characterized employing SEM, DLS, physisorption techniques, and XRD. By adsorbing CNDs, L1, and the CND-L1 hybrid onto TiO_2, three distinct sensitized catalysts were generated and subjected to further examination using XPS, TGA, and diffuse reflectance spectroscopy. Notably, CND-L1 hybrid exhibited near-complete adsorption on the TiO_2 surface, in contrast to the less effective attachment of the pure L1 dye and CNDs.

The photocatalytic degradation of MO was evaluated across all three sensitized catalysts in comparison to TiO_2 alone. Each sensitized catalyst exhibited enhanced degradation efficiency relative to TiO_2. Reusability studies demonstrated that while the CND exhibited the greatest stability of the sensitizers over time, the activity of the catalysts containing L1 dye diminished. Despite containing 24 times more L1 in the TiO_2-L1 catalyst than in the TiO_2-CND-L1 variant, the latter appeared to exhibit a higher TON.

The results of scavenger experiments highlighted the crucial roles of holes and hydroxyl radicals in the MO degradation mechanisms. Despite the fact that efforts to quantify $^\bullet O_2{}^-$ radical levels using *p*-BQ and AA as scavengers yielded inconclusive results, thereby leaving open the possibility that superoxide anions play a pivotal role in the catalysis, it was evident that the addition of AA improved degradation efficiency for both TiO_2 and TiO_2-CND catalysts. In contrast, TiO_2-L1 and TiO_2-CND-L1 approached nearly 100% degradation without AA addition.

In summary, the synthesis of CND hybrid materials presents a promising strategy for enhancing dye adsorption on TiO_2 while minimizing dye usage. This approach not only enhances catalyst stability during catalysis but also offers potential cost savings by reducing reliance on expensive dyes due to the economical synthesis of CNDs. Furthermore, the presence of CNDs facilitates hole generation within both pristine and functionalized states in catalysts. This study provides a firm basis for future research into additional

hybrid materials with diverse dyes and optimization of reaction conditions with the aim of achieving more efficient pollutant degradation.

4. Materials and Methods

Citric acid (CA, $\geq$99.5%), 3-([(ethylimino)methylidene]amino)-*N*, *N*-dimethylpropan-1-amine hydrochloride (EDC, $\geq$99%), tetrakis(triphenylphosphin)palladium(0) ($\geq$98%), and ethylenediamine (EDA, $\geq$99.5%) were purchased from Carl-Roth (Karlsruhe, Germany). *N*-hydroxysuccinimide (NHS, $\geq$99%), ammonium acetate ($\geq$98%), and cesium carbonate (99.9%) were purchased from Sigma-Aldrich (St. Louis, MO, USA). Bromothiophene-2-carbaldehyde (>97%) was purchased from TCI (Zwijndrecht, Belgium). Triphenylamino boronic acid (98%) was purchased from BLDpharm (Shanghai, China). Cyanoacetic acid (97%), and titanium(IV) chloride (99.9%) were purchased from Thermo Scientific (Waltham, MA, USA). Glacial acetic acid (99–100%) was purchased from VWR Chemicals (Radnor, PA, USA). Deuterated dimethyl sulfoxide (DMSO-d6, 99.8%), chloroform (CDCl$_3$-d, 99.8%), and acetone-d6 (99.8%) were purchased from Deutero (Sejong-si, Republic of Korea). Anhydrous *N,N*-dimethylformamide (DMF, 99.8%, AcroSeal) and tetrahydrofuran (THF, 99.5%, AcroSeal) were purchased from Thermo Scientific (Waltham, MA, USA). Dimethylsulfoxide (DMSO, 99.5%) was purchased from Gruessing (Filsum, Germany). Solvents for UV-Vis and PL spectroscopy was purchased from Merck (Darmstadt, Germany) (Uvasol® quality). Ultrapure water was obtained with the Milli-Q Direct Water Purification System. Unless otherwise stated, the reagents were used without further purification. The MW-assisted reactions were performed in a Silvia homeline set-up. The purification of CNDs was performed with Cytiva (Marlborough, MA, USA) Sephadex G-10 and LH-20 gel filtration media for size-exclusion chromatography. NMR-spectra were recorded with a Avance II 400 MHz, and Avance III 400 MHz HD (both Bruker, Ettlingen, Germany). Diffusion measurements were performed using an AVANCE III HD 400 MHz NMR spectrometer equipped with a gradient probe head ("Diff50", Bruker, Ettlingen, Germany) with a selective ^{1}H insert, providing a magnetic field gradient strength of up to 28 T m^{-1}. The samples were measured at 25 °C. To calibrate the temperature a PT 100 thermocouple inserted in an NMR tube, filled with oil, was used. UV-Vis measurements were carried out with a SPECORD® 200 PLUS spectrophotometer equipped with two automatic eight-fold cell changers and a Peltier element thermostat system (0.1 °C accuracy) by Analytik Jena (Jena, Germany). The system was operated with the ASpect UV 2.0 software by Analytik Jena. Fluorescence measurements were conducted with a Jasco (Heckmondwike, UK) FP-8300 Fluorescence Spectrometer. The sample solutions were measured in QS High Precision Cells made of Quartz Suprasil® with a light path of 10 mm by Hellma Analytics (Muellheim, Germany). Experiments were carried out in concentrations of 6–14 mg L^{-1}. Stock solutions (1 mg mL^{-1}) were prepared from freshly purified samples, and then diluted prior to every UV/Vis and PL experiment. The spectra of the L1 dye was obtained using 0.5–2.5 μmol L^{-1} solutions in DMSO at 25 °C. UV-Vis spectra of catalysis were recorded using a Bio-Tek Uvikon XS Spectrophotometer by Agilent (Santa Clara, CA, USA), controlled by UV VISion 1.0 Lite software. The sample solutions were measured in QS High Precision Cells made of Quartz Suprasil® with a light path of 1.0 mm by Hellma Analytics (Muellheim, Germany). Diffuse reflectance spectra were recorded using a Cary 5000 UV-Vis-NIR spectrophotometer by Agilent (Santa Clara, CA, USA) in conjunction with the Cary WinUV Scan Application software (ver. 6.3.0.1595) from Agilent Technologies (Santa Clara, CA, USA). The spectrophotometer was equipped with a Praying Mantis™ Diffuse Reflectance Accessory from Harrick Scientific Products (Pleasantville, NY, USA) and operated in double beam mode, with a reduced slit for white samples and full slit for colored samples. The data was collected in reflectance units, as this method is relative, hence Polytetrafluoroethylene (PTFE)

was selected as the reference material. Both the reference and the samples were ground and loaded into a DRP-SAP microsample-cup (Harrick Scientific Products (Pleasantville, NY, USA)) and flattened with a spatula. Elemental analysis (CHNS) was performed using the Organic elemental analyzer UNICUBE (Langenselbold, Germany). The residual percentage in EA was assumed to be oxygen for pristine materials and TiO_2 for the nanocomposites. XRD was performed on a XRDynamic 500 difractometer by Anton Paar (Graz, Austria) in the range of 20–90° with a step size of 0.01° and 100.364 s per step. XPS measurements were conducted using a PHI 5000 VersaProbe IV Scanning ESCA Microprobe by Physical Electronics (Chanhassen, MN, USA) with a monochromatized Al Kα X-ray source (1486.6 eV, 100 μm beam diameter, 25 W power, and 15 kV voltage). The samples were prepared in PTFE sample caps and attached to the XPS holder using insulating tape. During the measurements, charge neutralization was achieved using slow electrons and argon ions, and pressure was maintained between 10^{-7} and 10^{-6} Pa. Spectral data were analyzed using CasaXPS software (Version 2.3.25PR 1.0). Dynamic light scattering (DLS) measurements were performed at 20 °C using a Malvern Zetasizer Nano-ZS device (Malvern, UK), operated with Malvern Panalytical's Zetasizer software 7.13. SEM images were recorded using a GeminiSEM 560 microscope by Zeiss (Oberkochen, Germany) with an InLens detector. For working distance, a range of 2.4 to 2.6 mm and an acceleration voltage of 1 kV was used. All samples were sputter-coated with platinum using a Leica EM ACE600 sputter coater (Wetzlar, Germany) in order to increase the conductivity of the specimens. Fiji ImageJ 1.54 software was used utilized for image evaluation. Nitrogen physisorption experiments were performed using a Quadrasorb evo instrument by Quantachrome Instruments (Graz, Austria) at a temperature of 77 K. Pore size distributions were calculated using an NLDFT kernel (N_2 at 77 K, silica, cylindr. pores, adsorption branch). Atomic force microscopy (AFM) was performed in AC mode using an AIST-NT (Novato, CA, USA) SmartSPM 1000 under ambient conditions. 0.02 mg mL^{-1} dispersions of CNDs in DMSO were drop casted on freshly cleaved V1 grade Mica discs (10 mm diameter, 0.15–0.21 mm thickness). The AFM utilized a SSS-FMR probe by NANOSENSORS (Neuchatel, Switzerland), a super sharp silicon tip apex, and an aluminum-coated detector side (75 kHz, 2.8 N m^{-1}). Data analysis was carried out using Gwyddion 2.62 software. Thermogravimetric analysis (TGA) was conducted using a Luxx STA 409 PC Simultaneous thermal analyzer (Netzsch, Selb, Germany) with coupled mass spectrometry QMS 403 C Aeolos (Netzsch, Selb, Germany). Prior to the measurement ramp (10 °C min^{-1} from 100 °C to 900 °C) under argon or synthetic air atmospheres, pristine samples underwent isothermal desorption of adsorbed moisture under Ar (60 °C for 10 min, followed by 80 °C for 3 min and 100 °C for 2 min). For titania-based materials, measurements were taken without any prior treatment.

4.1. CND Synthesis

For the sake of clarity, the details of the already reported and slightly modified method reported by Pham et al. [35] are given here. CA (1.4410 g, 7.50 mmol, 1 eq.) was dissolved in 5 mL Milli-Q water and was stirred until the substrate was completely dissolved. EDA (0.50 mL, 7.5 mmol, 1 eq.) was added and the mixture was stirred for 20 min. The reaction mixture was heated in a domestic MW oven for five minutes at 400 W (50% power). The obtained brown resin was dispersed in 4 mL Milli-Q water, filtered through a 0.2 μm PTFE syringe filter, and purified using a Sephadex LH-20 gel column with Milli-Q water as eluent. The obtained brown dispersion was lyophilized and an orange/brown solid was obtained. Yield: 0.3734 g, 20 wt%.

^{1}H-NMR of the CND species showed broad signals to ensure the presence of CNDs (Figure S38) [62].

4.2. 5-(4-(Diphenylamino)phenyl)thiophene-2-Carbaldehyde

Bromothiophene-2-carbaldehyde (1.200 g, 6.28 mmol, 1.0 eq.), triphenylamino boronic acid (2.0017 g, 6.92 mmol, 1.1 eq.), cesium carbonate (4.1120 g, 12.6 mmol, 2.0 eq.), and Tetrakis(triphenylphosphin)palladium(0) (0.3625 g, 0.31 mmol, 0.05 eq.) were dissolved in 40 mL dry THF and 6.3 mL water, and refluxed overnight under an argon atmosphere. The reaction mixture was cooled to room temperature, diluted with DCM and water. The mixture was extracted three times with DCM and the organic phase was combined and dried over $MgSO_4$, filtered, and the solvent was removed under reduced pressure. The resulting yellow crude product was purified by column chromatography using DCM: n-hexane (1:1) as an eluent, which was subsequently changed to DCM after the elution of the starting material. A yellow crystalline solid was obtained as the final product.

Yield: 1.9043 g, 85%.

^{1}H-NMR (400 MHz, Chloroform-d): δ = 9.86 (s, 1H), 7.71 (d, *J* = 4.0 Hz, 1H), 7.55–7.49 (m, 2H), 7.34–7.27 (m, 5H), 7.14 (d, *J* = 7.5 Hz, 4H), 7.10 (d, *J* = 7.3 Hz, 2H), 7.06 (d, *J* = 8.7 Hz, 2H) ppm.

Analytical data corresponded to the literature [63].

4.3. 2-Cyano-3-(5-(4-(diphenylamino)phenyl)thiophen-2-yl)acrylic Acid (L1)

5-(4-(Diphenylamino)phenyl)thiophene-2-carbaldehyde (0.6012 g, 1.69 mmol, 1.0 eq.), cyanoacetic acid (0.7195 g, 8.46 mmol, 5.0 eq.), and ammonium acetate (0.3315 g, 4.30 mmol, 2.5 eq.) were dissolved in 105.5 mL glacial acetic acid, and refluxed overnight. The reaction mixture was cooled to room temperature and the solvent was removed by distillation under reduced pressure. The resulting purple crude product was purified by column chromatography using DCM: methanol (10:1) as an eluent. A red solid was obtained as the final product.

Yield: 0.6508 g, 84%.

^{1}H-NMR (400 MHz, Acetone-d6): δ = 8.43 (s, 1H), 7.96 (d, *J* = 4.1 Hz, 1H), 7.72 (d, *J* = 8.8 Hz, 2H), 7.61 (d, *J* = 4.0 Hz, 1H), 7.37 (dd, *J* = 8.8, 7.0 Hz, 4H), 7.16 (d, *J* = 7.7 Hz, 6H), 7.06 (d, *J* = 8.8 Hz, 2H) ppm.

Analytical data corresponded to the literature [64].

4.4. Amide Coupling of CND with L1

L1 (0.6670 g, 1.54 mmol, 1.0 eq.), *N*-hydroxysuccinimide (0.3642 g, 3.16 mmol, 2 eq.), and *N*-(3-Dimethylaminopropyl)-*N′*-ethylcarbodiimid -hydrochlorid (0.6061 g, 3.16 mmol, 2.0 eq.) were dissolved in 130 mL dry DMF in a 250 mL Schlenk round bottom flask and stirred at room temperature for 30 min under argon atmosphere. CND (0.3790 g) was added and the reaction mixture was stirred at room temperature for two days under argon atmosphere. The solvent was removed under reduced pressure. The dark-red resin was dispersed in DCM: methanol (10:1) and packed on a silica gel glass frit. Then it was washed with DCM: methanol (10:1) to remove any side products and precursors until the solvent had little to no color after washing. The product adsorbed on the silica was washed off with DMSO and then freeze-dried. Further purification was carried out using a Sephadex G-10 gel column with DMSO as eluent. The obtained red/brown dispersion was lyophilized and a red/brown solid was obtained.

4.5. TiO₂-Particle Synthesis

The synthesis proceeded with modification after Yeh et al. [50]. Under Schlenk conditions titanium tetrachloride (12 mL, 21 g, 110 mmol) were added into a three neck round bottom flask and 240 mL Milli-Q water were added dropwise, stirred, and cooled with a cooling bath of acetonitrile and liquid nitrogen. Formed HCl gas was captured by using

NaOH solution in a washing flask. Following the absence of a reaction upon the further addition of Milli-Q water, the reaction mixture was stirred for one hour. By addition of aqueous ammonia (25%) the pH of the solution was adjusted to 7. The white precipitate was washed with copious amounts of Milli-Q water to remove any soluble residues and dried at 40 °C overnight. The obtained colorless powder was then calcinated for 10 h at 350 °C with a heating rate of 2 °C min^{-1}.

4.6. TiO$_2$-Sensitized Catalyst

TiO$_2$ (500 mg, 6.26 mmol) was dispersed with 2 mg sensitizer (CND, L1 dye, CND-L1 hybrid) in 1 mL of acetonitrile, followed by sonication for 45 min. After this, an additional 10 mg of sensitizer was added, and sonication for another 45 min to ensure complete adsorption of the sensitizer onto TiO$_2$. The sonication process was conducted while cooling the sonication bath with ice to maintain room temperature. After adsorption, the dispersions were centrifuged for five minutes to remove acetonitrile. The catalyst underwent a three-stage wash process using water and centrifugation to remove water-soluble residues. The catalyst was dried overnight under reduced pressure.

4.7. Photocatalytic Procedure

Photocatalytic degradation was measured at 22.5 °C. 10 mg of catalyst was added to a 10 mL aqueous methyl orange (MO) solution (50 μM) and stirred for 30 min in dark. The pH of MO-solution was 6.5. For the catalysis a beaker with continuous cooling at 22.5 °C and an UV LED (Figure S19) has been used. The light intensity on the surface of the solution is 270 μW cm^{-2} at a distance of 16 cm. A single catalysis cycle was conducted over a period of 50 min, with 250 μL aliquots being sampled at 10-min intervals and subsequently subjected to centrifugation for 15 min. The extent of the degradation process was determined by measuring the UV-Vis absorbance of the solution of degraded MO in the wavelength range of 300–700 nm, with the maximum absorbance observed at 464 nm.

4.8. Reusability Procedure

Photocatalytic degradation was measured at 22.5 °C. 10 mg of catalyst was added to a 10 mL aqueous MO solution (50 μM) and stirred for 30 min in dark. The pH of MO-solution was 6.5. For the catalysis a beaker with continuous cooling at 22.5 °C and a UV LED (Figure S19) has been used. The light intensity on the surface of the solution is 270 μW cm^{-2} at a distance of 16 cm. A single catalysis cycle was conducted over a period of 50 min, with 250 μL aliquots being sampled at t_0 and t_{50} and subsequently subjected to centrifugation for 15 min. The extent of the degradation process was determined by measuring the UV-Vis absorbance of the solution in a 1.0 mm Hellma QS cuvette of degraded MO in the wavelength range of 300–700 nm, with the maximum absorbance observed at 464 nm. The extent of colorant degradation was determined through the use of UV-Vis spectrometry. Following irradiation, the suspension was transferred into a centrifuge tube and subjected to centrifugation. The supernatant was removed, and the catalyst was washed with water. After centrifuging and removing the water, the catalyst was dried under reduced pressure overnight. The residual amount of catalyst was then reused with 1 mL MO solution per 1 mg catalyst, and the procedure was repeated three times in total to determine the change in degradation efficiency after each catalytic cycle.

4.9. Scavenger Procedure

A total of 10 mg of the respective photocatalyst were dispersed in 10 mL MO solution (50 μM in milliQ®). Then, 10 mg of one of the scavenger substances was added (IPA, *p*-BQ, AA, EDTA). The respective mixtures exhibited the following pH values: 5.7 for IPA, 4.8 for EDTA, and 3.0 for AA. The dispersion was stirred in the dark for 30 min at 22.5 °C before

irradiation with the LED for 50 min. Before and after irradiation an aliquot of 250 µL was taken, centrifuged for 15 min and measured with the UV-Vis spectrometer. For analysis the absorbance [a.u.] of $\lambda_{\mathrm{MO,max}}$ = 464 nm (pH < 4.4) [65] and $\lambda_{\mathrm{MO,max}}$ = 517 nm (pH > 4.4) [66] was used.

Supplementary Materials: The following supporting information can be downloaded at: https://www.mdpi.com/article/10.3390/photochem5010001/s1. Figure S1. (A) The 2D AFM image (1000 × 1000 nm) of CND is presented, with an inset showing the mean height and standard deviation of approximately 70 CNDs. (B) 2D AFM image (500 × 500 nm) of CND. (C) Height profile along the white line in the 500 × 500 nm 2D image. (D) 3D AFM image (500 × 500 nm) of CND. Figure S2. 2D DOSY NMR spectra of L1 dye measured in DMSO-d6. Figure S3. 2D DOSY NMR spectra of CND measured in DMSO-d6. Figure S4. 2D DOSY NMR spectra of a physical mixture of CND (10 mg·mL^{-1}) and L1 (1 mg·mL^{-1}) measured in DMSO-d6. Figure S5. 2D DOSY NMR spectra of CND-L1 hybrid measured in DMSO-d6.; Figure S6. (A) UV-Vis absorbance (solid lines) and PL intensity (dashed lines, λ_{Exc} = 360 nm) of five different CND dispersions. (B) UV-Vis absorbance (solid lines) and PL intensity (dashed lines, λ_{Exc} = 412 nm) of five different concentrated L1 solutions. (C) UV-Vis absorbance (solid lines) and PL intensity (dashed lines, λ_{Exc} = 362 nm) of five different concentrated CND-L1 dispersions. (D) UV-Vis absorbance (solid lines) and PL intensity (dashed lines, λ_{Exc} = 340 nm) of five different concentrated QS solutions. (E) Absorbance maxima plotted against the integrated PL intensity of the five different concentrations and the respective slopes derived from a linear fit. Figure S7. UV-Vis absorbance at 412 nm of five different concentrated CND, L1, and CND-L1 solutions and the respective slopes which correspond to the absorption coefficient derived from a linear fit. The UV-Vis absorbance at 412 nm of five different concentrated CND, L1, and CND-L1 solutions/dispersions, along with the corresponding slopes, were obtained from a linear fit and correspond to the absorption coefficient ε_{λ}. Figure S8. Excitation-emission maps recorded in an excitation wavelength range of 260 nm to 650 nm and an emission wavelength range of 280 nm to 720 nm. (A) CND with a concentration of 6 mg · L^{-1} in DMSO. (B) L1 with a concentration of 1.0 µM in DMSO. (C) CND-L1 with a concentration of 6 mg · L^{-1} in DMSO. Figure S9. Excitation spectra recorded in the excitation wavelength range of 260 nm to 700 nm. (A) CND with a concentration of 6 mg · L^{-1} in DMSO at an emission wavelength of 440 nm. (B) L1 with a concentration of 1.0 µM in DMSO at an emission wavelength of 559 nm. (C) CND-L1 with a concentration of 6 mg · L^{-1} in DMSO at an emission wavelength of 445 nm. Figure S10. TGA analysis of the CNDs measured in argon (A) CND in comparison to L1 and CND-L1. (B) Derived weight loss of CND in comparison to L1 and CND-L1. In all cases, the first significant weight loss was observed between 100 °C and 300 °C. Furthermore, the CND-L1 hybrid showed higher weight loss in this range. Decomposition started at around 350 °C. Figure S11. XPS Survey-spectra for (A) CND, (B) L1 dye, and (C) CND-L1 hybrid respectively. (D) The atomic ratios were obtained from XPS measurements. (E) Elemental composition determined through elemental analysis (EA), highlighting the overall composition of the materials. (F) The element composition (from EA) is given without hydrogen, so that a direct comparison with the XPS atomic ratios is possible. Figure S12. Deconvoluted absorbance spectrum of CND-L1 (14 mg·L^{-1} in DMSO) with four Gaussian-shaped functions. For Peak 1 (CND), the wavelength was fixed at 265 nm. For Peak 2 (L1), the wavelength was fixed at 302 nm. For Peak 3 (CND), the wavelength was fixed at 357 nm. For Peak 4 (L1), the wavelength was fixed at 454 nm. A maximum absorbance of 0.0291 was obtained for Peak 4 (L1). This indicates that 2.2% of the CND-L1 hybrid represents the L1 dye component. Figure S13. (A) Nitrogen (77 K) isotherm of TiO$_2$ particles and (B) their pore size distribution obtained by applying a non-local density functional theory (NLDFT) kernel for cylindrical pore geometries on the adsorption branch. Figure S14. (A+B) SEM images showing particles of (31 ± 5) nm and agglomerated particles. (B) Insert: aggregated particles in an aqueous solution, with an average diameter of (685 ± 160) nm, as determined by dynamic light scattering (DLS). Figure S15. The XRD pattern of the TiO$_2$ particles is in accordance with the standard data file (ICSD Card No. 98-018-4368) for pure anatase TiO$_2$. No additional reflections are present other than those illustrated in the reference card. Figure S16. $(F(R_\infty)h\nu)^{1/\gamma}$ plotted against hν for the pristine TiO$_2$ particles with linear extrapolation for band gap energy E_{g} determination. Figure S17. XPS Survey-spectra for

(A) TiO_2, (B) TiO_2-CND, (C) TiO_2-L1, and (D) TiO_2-CND-L1 respectively. (E) The atomic ratios were obtained from XPS measurements and compared with the previously determined values of the materials without TiO_2. Figure S18. TGA analysis was conducted on both the TiO_2 particles and the sensitized ones, which were measured in synthetic air. Figure S19. Emission spectra of the employed 395 nm LED Chip. YXO YUXINOU COB Chip, 220 V AC voltage, and 50 W power. The light intensity on the surface of the solution is 270 $\mu W \cdot cm^{-2}$ at a distance of 16 cm. Table S1: TiO_2-CND-L1 values from reusability experiments for TON/TOF calculation. Table S2: TiO_2-L1 values from reusability experiments for TON/TOF calculation. Figure S20. The appearance of 10 mg of the TiO_2 catalyst in 10 mL of a MO solution (aqueous, 50 μM) following irradiation is illustrated. Figure S21. Degradation efficiency of each catalyst for MO photodegradation at pH 3.0, acidified with HCl, compared to degradation efficiency with AA as scavenger at pH 3.0. Figure S22. UV-Vis absorbance spectra for the three runs of catalytic MO-degradation over a period of 50 minutes with TiO_2 catalyst. Figure S23. UV-Vis absorbance spectra for the three runs of catalytic MO-degradation over a period of 50 minutes with TiO_2-CND catalyst. Figure S24. UV-Vis absorbance spectra for the three runs of catalytic MO-degradation over a period of 50 minutes with TiO_2-L1 catalyst. Figure S25. UV-Vis absorbance spectra for the three runs of catalytic MO-degradation over a period of 50 minutes with TiO_2-CND-L1 catalyst. Figure S26. UV-Vis absorbance spectra for the three runs of catalytic MO-degradation over a period of 50 minutes with TiO_2 catalyst without light irradiation. Figure S27. UV-Vis absorbance spectra for the three runs of catalytic MO-degradation over a period of 50 minutes with TiO_2-CND catalyst without light irradiation. Figure S28. UV-Vis absorbance spectra for the three runs of catalytic MO-degradation over a period of 50 minutes with TiO_2-L1 catalyst without light irradiation. Figure S29. UV-Vis absorbance spectra for the three runs of catalytic MO-degradation over a period of 50 minutes with TiO_2-CND-L1 catalyst without light irradiation. Figure S30. UV-Vis absorbance spectra of catalytic MO-degradation over a period of 50 minutes per cycle with TiO_2 catalyst. (A) First measurement; (B) second measurement: (C) third measurement. Figure S31. UV-Vis absorbance spectra of catalytic MO-degradation over a period of 50 minutes per cycle with TiO_2-CND catalyst. (A) First measurement; (B) second measurement: (C) third measurement. Figure S32. UV-Vis absorbance spectra of catalytic MO-degradation over a period of 50 minutes per cycle with TiO_2-L1 catalyst. (A) First measurement; (B) second measurement: (C) third measurement. Figure S33. UV-Vis absorbance spectra of catalytic MO-degradation over a period of 50 minutes per cycle with TiO_2-CND-L1 catalyst. (A) First measurement; (B) second measurement: (C) third measurement. Figure S34. UV-Vis absorbance spectra of catalytic MO-degradation over a period of 50 minutes per cycle with AA acting as the scavenger. (A) TiO_2; (B) TiO_2-CND; (C) TiO_2-L1; (D) TiO_2-CND-L1. Figure S35. UV-Vis absorbance spectra of catalytic MO-degradation over a period of 50 minutes per cycle with EDTA acting as the scavenger. (A) TiO_2; (B) TiO_2-CND; (C) TiO_2-L1; (D) TiO_2-CND-L1. Figure S36. UV-Vis absorbance spectra of catalytic MO-degradation over a period of 50 minutes per cycle with IPA acting as the scavenger. (A) TiO_2; (B) TiO_2-CND; (C) TiO_2-L1; (D) TiO_2-CND-L1. Figure S37. UV-Vis absorbance spectra of catalytic MO-degradation over a period of 50 minutes per cycle without a scavenger at pH 3.0. (A) TiO_2; (B) TiO_2-CND; (C) TiO_2-L1; (D) TiO_2-CND-L1. Figure S38. ^{1}H-NMR spectra of CND measured in DMSO-d6. Figure S39. ^{1}H-NMR spectra of 5-(4-(Diphenylamino)phenyl)thiophene-2-carbaldehyde measured in Chloroform-d1. Figure S40. ^{1}H-NMR spectra of 2-Cyano-3-(5-(4-(diphenylamino)phenyl)thiophen-2-yl)acrylic acid measured in Acetone-d6. Figure S41. ^{1}H-NMR spectra of CND-L1 Hybrid measured in DMSO-d6. References [39,40,51,52,65,67–71] are cited in the Supplementary Materials.

Conflicts of Interest: The authors declare no conflicts of interest.

References

1. Dutta, S.; Adhikary, S.; Bhattacharya, S.; Roy, D.; Chatterjee, S.; Chakraborty, A.; Banerjee, D.; Ganguly, A.; Nanda, S.; Rajak, P. Contamination of Textile Dyes in Aquatic Environment: Adverse Impacts on Aquatic Ecosystem and Human Health, and Its Management Using Bioremediation. *J. Environ. Manag.* **2024**, *353*, 120103. [CrossRef]

2. Bailey, K.; Basu, A.; Sharma, S. The Environmental Impacts of Fast Fashion on Water Quality: A Systematic Review. *Water* **2022**, *14*, 1073. [CrossRef]

3. Singh, P. (Ed.) *Dye Pollution from Textile Industry: Challenges and Opportunities for Sustainable Development*; SDGs and Textiles; Springer Nature: Singapore, 2024. [CrossRef]

4. Khan, R.R.M.; Qamar, H.; Hameed, A.; ur Rehman, A.; Pervaiz, M.; Saeed, Z.; Adnan, A.; Ch, A.R. Biological and Photocatalytic Degradation of Congo Red, a Diazo Sulfonated Substituted Dye: A Review. *Water Air Soil Pollut.* **2022**, *233*, 468. [CrossRef]

5. Pandey, A.; Singh, P.; Iyengar, L. Bacterial Decolorization and Degradation of Azo Dyes. *Int. Biodeterior. Biodegrad.* **2007**, *59*, 73–84. [CrossRef]

6. Garcia, B.B.; Lourinho, G.; Romano, P.; Brito, P.S.D. Photocatalytic Degradation of Swine Wastewater on Aqueous TiO_2 Suspensions: Optimization and Modeling via Box-Behnken Design. *Heliyon* **2020**, *6*, e03293. [CrossRef]

7. Lin, Y.P.; Mehrvar, M. Photocatalytic Treatment of An Actual Confectionery Wastewater Using $Ag/TiO_2/Fe_2O_3$: Optimization of Photocatalytic Reactions Using Surface Response Methodology. *Catalysts* **2018**, *8*, 409. [CrossRef]

8. Jain, K.; Patel, A.S.; Pardhi, V.P.; Flora, S.J.S. Nanotechnology in Wastewater Management: A New Paradigm Towards Wastewater Treatment. *Molecules* **2021**, *26*, 1797. [CrossRef] [PubMed]

9. Goodeve, C.F.; Kitchener, J.A. The Mechanism of Photosensitisation by Solids. *Trans. Faraday Soc.* **1938**, *34*, 902–908. [CrossRef]

10. Ahmed, S.N.; Haider, W. Heterogeneous Photocatalysis and Its Potential Applications in Water and Wastewater Treatment: A Review. *Nanotechnology* **2018**, *29*, 342001. [CrossRef]

11. Anwer, H.; Mahmood, A.; Lee, J.; Kim, K.-H.; Park, J.-W.; Yip, A.C.K. Photocatalysts for Degradation of Dyes in Industrial Effluents: Opportunities and Challenges. *Nano Res.* **2019**, *12*, 955–972. [CrossRef]

12. Rani, P.; Kumar, V.; Singh, P.P.; Matharu, A.S.; Zhang, W.; Kim, K.-H.; Singh, J.; Rawat, M. Highly Stable AgNPs Prepared via a Novel Green Approach for Catalytic and Photocatalytic Removal of Biological and Non-Biological Pollutants. *Environ. Int.* **2020**, *143*, 105924. [CrossRef] [PubMed]

13. Koe, W.S.; Lee, J.W.; Chong, W.C.; Pang, Y.L.; Sim, L.C. An Overview of Photocatalytic Degradation: Photocatalysts, Mechanisms, and Development of Photocatalytic Membrane. *Environ. Sci. Pollut. Res.* **2020**, *27*, 2522–2565. [CrossRef] [PubMed]

14. Neppolian, B.; Choi, H.C.; Sakthivel, S.; Arabindoo, B.; Murugesan, V. Solar/UV-Induced Photocatalytic Degradation of Three Commercial Textile Dyes. *J. Hazard. Mater.* **2002**, *89*, 303–317. [CrossRef] [PubMed]

15. Gatou, M.-A.; Syrrakou, A.; Lagopati, N.; Pavlatou, E.A. Photocatalytic TiO_2-Based Nanostructures as a Promising Material for Diverse Environmental Applications: A Review. *Reactions* **2024**, *5*, 135–194. [CrossRef]

16. Lee, S.-Y.; Park, S.-J. TiO_2 Photocatalyst for Water Treatment Applications. *J. Ind. Eng. Chem.* **2013**, *19*, 1761–1769. [CrossRef]

17. Hassan, N.S.; Jalil, A.A.; Khusnun, N.F.; Bahari, M.B.; Hussain, I.; Firmansyah, M.L.; Nugraha, R.E.; Rajendran, S. Extra-Modification of Zirconium Dioxide for Potential Photocatalytic Applications towards Environmental Remediation: A Critical Review. *J. Environ. Manag.* **2023**, *327*, 116869. [CrossRef] [PubMed]

18. Luís, A.M.; Neves, M.C.; Mendonça, M.H.; Monteiro, O.C. Influence of Calcination Parameters on the TiO_2 Photocatalytic Properties. *Mater. Chem. Phys.* **2011**, *125*, 20–25. [CrossRef]

19. Mohd Abdah, M.A.A.; Azman, N.H.N.; Kulandaivalu, S.; Sulaiman, Y. Review of the Use of Transition-Metal-Oxide and Conducting Polymer-Based Fibres for High-Performance Supercapacitors. *Mater. Des.* **2020**, *186*, 108199. [CrossRef]

20. Ananthakumar, S.; Balaji, D.; Ram Kumar, J.; Moorthy Babu, S. Role of Co-Sensitization in Dye-Sensitized and Quantum Dot-Sensitized Solar Cells. *SN Appl. Sci.* **2019**, *1*, 186. [CrossRef]

21. Park, H.; Park, Y.; Kim, W.; Choi, W. Surface Modification of TiO₂ Photocatalyst for Environmental Applications. *J. Photochem. Photobiol. C Photochem. Rev.* **2013**, *15*, 1–20. [CrossRef]

22. Wang, C.; Li, J.; Mele, G.; Yang, G.-M.; Zhang, F.-X.; Palmisano, L.; Vasapollo, G. Efficient Degradation of 4-Nitrophenol by Using Functionalized Porphyrin-TiO₂ Photocatalysts under Visible Irradiation. *Appl. Catal. B Environ.* **2007**, *76*, 218–226. [CrossRef]

23. Youssef, Z.; Colombeau, L.; Yesmurzayeva, N.; Baros, F.; Vanderesse, R.; Hamieh, T.; Toufaily, J.; Frochot, C.; Roques-Carmes, T.; Acherar, S. Dye-Sensitized Nanoparticles for Heterogeneous Photocatalysis: Cases Studies with TiO₂, ZnO, Fullerene and Graphene for Water Purification. *Dyes Pigment.* **2018**, *159*, 49–71. [CrossRef]

24. Cherian, S.; Wamser, C.C. Adsorption and Photoactivity of Tetra(4-Carboxyphenyl)Porphyrin (TCPP) on Nanoparticulate TiO₂. *J. Phys. Chem. B* **2000**, *104*, 3624–3629. [CrossRef]

25. Xu, X.; Ray, R.; Gu, Y.; Ploehn, H.J.; Gearheart, L.; Raker, K.; Scrivens, W.A. Electrophoretic Analysis and Purification of Fluorescent Single-Walled Carbon Nanotube Fragments. *J. Am. Chem. Soc.* **2004**, *126*, 12736–12737. [CrossRef]

26. Cayuela, A.; Soriano, M.L.; Carrillo-Carrión, C.; Valcárcel, M. Semiconductor and Carbon-Based Fluorescent Nanodots: The Need for Consistency. *Chem. Commun.* **2016**, *52*, 1311–1326. [CrossRef]

27. Pan, D.; Zhang, J.; Li, Z.; Wu, M. Hydrothermal Route for Cutting Graphene Sheets into Blue-Luminescent Graphene Quantum Dots. *Adv. Mater.* **2010**, *22*, 734–738. [CrossRef]

28. Debes, P.P.; Langer, M.; Pagel, M.; Menna, E.; Smarsly, B.; Osella, S.; Gallego, J.; Gatti, T. Functional Groups Accessibility and the Origin of Photoluminescence in N/O-Containing Bottom-up Carbon Nanodots. *ChemNanoMat* **2024**, *10*, e202300471. [CrossRef]

29. Langer, M.; Zdražil, L.; Medveď, M.; Otyepka, M. Communication of Molecular Fluorophores with Other Photoluminescence Centres in Carbon Dots. *Nanoscale* **2023**, *15*, 4022–4032. [CrossRef]

30. Jorns, M.; Pappas, D. A Review of Fluorescent Carbon Dots, Their Synthesis, Physical and Chemical Characteristics, and Applications. *Nanomaterials* **2021**, *11*, 1448. [CrossRef] [PubMed]

31. Filippini, G.; Amato, F.; Rosso, C.; Ragazzon, G.; Vega-Peñaloza, A.; Companyó, X.; Dell'Amico, L.; Bonchio, M.; Prato, M. Mapping the Surface Groups of Amine-Rich Carbon Dots Enables Covalent Catalysis in Aqueous Media. *Chem* **2020**, *6*, 3022–3037. [CrossRef]

32. Dinda, D.; Park, H.; Lee, H.-J.; Oh, S.; Park, S.Y. Graphene Quantum Dot with Covalently Linked Rhodamine Dye: A High Efficiency Photocatalyst for Hydrogen Evolution. *Carbon* **2020**, *167*, 760–769. [CrossRef]

33. Liu, Y.; Zhong, D.; Yu, L.; Shi, Y.; Xu, Y. Primary Amine Functionalized Carbon Dots for Dead and Alive Bacterial Imaging. *Nanomaterials* **2023**, *13*, 437. [CrossRef] [PubMed]

34. Gold, V. (Ed.) *The IUPAC Compendium of Chemical Terminology: The Gold Book*, 4th ed.; International Union of Pure and Applied Chemistry (IUPAC): Research Triangle Park, NC, USA, 2019. [CrossRef]

35. Pham, S.N.; Kuether, J.E.; Gallagher, M.J.; Hernandez, R.T.; Williams, D.N.; Zhi, B.; Mensch, A.C.; Hamers, R.J.; Rosenzweig, Z.; Fairbrother, H.; et al. Carbon Dots: A Modular Activity to Teach Fluorescence and Nanotechnology at Multiple Levels. *J. Chem. Educ.* **2017**, *94*, 1143–1149. [CrossRef]

36. Hagberg, D.P.; Marinado, T.; Karlsson, K.M.; Nonomura, K.; Qin, P.; Boschloo, G.; Brinck, T.; Hagfeldt, A.; Sun, L. Tuning the HOMO and LUMO Energy Levels of Organic Chromophores for Dye Sensitized Solar Cells. *J. Org. Chem.* **2007**, *72*, 9550–9556. [CrossRef]

37. Michaels, H.; Rinderle, M.; Freitag, R.; Benesperi, I.; Edvinsson, T.; Socher, R.; Gagliardi, A.; Freitag, M. Dye-Sensitized Solar Cells under Ambient Light Powering Machine Learning: Towards Autonomous Smart Sensors for the Internet of Things. *Chem. Sci.* **2020**, *11*, 2895–2906. [CrossRef]

38. Gomez, I.J.; Arnaiz, B.; Cacioppo, M.; Arcudi, F.; Prato, M. Nitrogen-Doped Carbon Nanodots for Bioimaging and Delivery of Paclitaxel. *J. Mater. Chem. B* **2018**, *6*, 5540–5548. [CrossRef] [PubMed]

39. Price, W.S. *NMR Studies of Translational Motion: Principles and Applications*; Cambridge Molecular Science; Cambridge University Press: Cambridge, UK, 2009. [CrossRef]

40. Lenoch, A.; Schumacher, M.; Gröschel, A.H.; Cramer, C.; Schönhoff, M. Diffusion NMR of Poly(Acrylic Acid) Solutions: Molar Mass Scaling and pH-Induced Conformational Variation. *Macromol. Chem. Phys.* **2023**, *224*, 2300286. [CrossRef]

41. Li, L.; Dong, T. Photoluminescence Tuning in Carbon Dots: Surface Passivation or/and Functionalization, Heteroatom Doping. *J. Mater. Chem. C* **2018**, *6*, 7944–7970. [CrossRef]

42. Cacioppo, M.; Scharl, T.; Đorđević, L.; Cadranel, A.; Arcudi, F.; Guldi, D.M.; Prato, M. Symmetry-Breaking Charge-Transfer Chromophore Interactions Supported by Carbon Nanodots. *Angew. Chem. Int. Ed.* **2020**, *59*, 12779–12784. [CrossRef]

43. Yildiz, I.; Tomasulo, M.; Raymo, F.M. A Mechanism to Signal Receptor–Substrate Interactions with Luminescent Quantum Dots. *Proc. Natl. Acad. Sci. USA* **2006**, *103*, 11457–11460. [CrossRef]

44. Sykora, M.; Petruska, M.A.; Alstrum-Acevedo, J.; Bezel, I.; Meyer, T.J.; Klimov, V.I. Photoinduced Charge Transfer between CdSe Nanocrystal Quantum Dots and Ru−Polypyridine Complexes. *J. Am. Chem. Soc.* **2006**, *128*, 9984–9985. [CrossRef] [PubMed]

45. Moroz, P.; Jin, Z.; Sugiyama, Y.; Lara, D.; Razgoniaeva, N.; Yang, M.; Kholmicheva, N.; Khon, D.; Mattoussi, H.; Zamkov, M. Competition of Charge and Energy Transfer Processes in Donor–Acceptor Fluorescence Pairs: Calibrating the Spectroscopic Ruler. *ACS Nano* **2018**, *12*, 5657–5665. [CrossRef] [PubMed]

46. Stewart, M.H.; Huston, A.L.; Scott, A.M.; Efros, A.L.; Melinger, J.S.; Gemmill, K.B.; Trammell, S.A.; Blanco-Canosa, J.B.; Dawson, P.E.; Medintz, I.L. Complex Förster Energy Transfer Interactions between Semiconductor Quantum Dots and a Redox-Active Osmium Assembly. *ACS Nano* **2012**, *6*, 5330–5347. [CrossRef]

47. Piston, D.W.; Kremers, G.-J. Fluorescent Protein FRET: The Good, the Bad and the Ugly. *Trends Biochem. Sci.* **2007**, *32*, 407–414. [CrossRef]

48. Valeev, E.F.; Coropceanu, V.; da Silva Filho, D.A.; Salman, S.; Brédas, J.-L. Effect of Electronic Polarization on Charge-Transport Parameters in Molecular Organic Semiconductors. *J. Am. Chem. Soc.* **2006**, *128*, 9882–9886. [CrossRef]

49. Brédas, J.L.; Calbert, J.P.; da Silva Filho, D.A.; Cornil, J. Organic Semiconductors: A Theoretical Characterization of the Basic Parameters Governing Charge Transport. *Proc. Natl. Acad. Sci. USA* **2002**, *99*, 5804–5809. [CrossRef] [PubMed]

50. Yeh, S.-W.; Ko, H.-H.; Chiang, H.-M.; Chen, Y.-L.; Lee, J.-H.; Wen, C.-M.; Wang, M.-C. Characteristics and Properties of a Novel in Situ Method of Synthesizing Mesoporous TiO_2 Nanopowders by a Simple Coprecipitation Process without Adding Surfactant. *J. Alloys Compd.* **2014**, *613*, 107–116. [CrossRef]

51. Kubelka, P.; Munk, F. Ein Beitrag Zur Optik Der Farbanstriche. *Z. Für Tech. Phys.* **1931**, *12*, 593–601.

52. Tauc, J.; Grigorovici, R.; Vancu, A. Optical Properties and Electronic Structure of Amorphous Germanium. *Phys. Status Solidi B* **1966**, *15*, 627–637. [CrossRef]

53. Nithiyanantham, U.; Ramadoss, A.; Ede, S.R.; Kundu, S. DNA Mediated Wire-like Clusters of Self-Assembled TiO_2 Nanomaterials: Supercapacitor and Dye Sensitized Solar Cell Applications. *Nanoscale* **2014**, *6*, 8010–8023. [CrossRef] [PubMed]

54. Vittadini, A.; Selloni, A.; Rotzinger, F.P.; Grätzel, M. Formic Acid Adsorption on Dry and Hydrated TiO_2 Anatase (101) Surfaces by DFT Calculations. *J. Phys. Chem. B* **2000**, *104*, 1300–1306. [CrossRef]

55. Khan, S.; Noor, T.; Iqbal, N.; Yaqoob, L. Photocatalytic Dye Degradation from Textile Wastewater: A Review. *ACS Omega* **2024**, *9*, 21751–21767. [CrossRef] [PubMed]

56. Tao, Y.; Han, Z.; Cheng, Z.; Liu, Q.; Wei, F.; Ting, K.E.; Yin, X.J. Synthesis of Nanostructured TiO_2 Photocatalyst with Ultrasonication at Low Temperature. *J. Mater. Sci. Chem. Eng.* **2015**, *3*, 29–36. [CrossRef]

57. Mondol, B.; Sarker, A.; Shareque, A.M.; Dey, S.C.; Islam, M.T.; Das, A.K.; Shamsuddin, S.M.; Molla, M.A.I.; Sarker, M. Preparation of Activated Carbon/TiO_2 Nanohybrids for Photodegradation of Reactive Red-35 Dye Using Sunlight. *Photochem* **2021**, *1*, 54–66. [CrossRef]

58. Zhang, Y.-Q.; Ma, D.-K.; Zhang, Y.-G.; Chen, W.; Huang, S.-M. N-Doped Carbon Quantum Dots for TiO_2-Based Photocatalysts and Dye-Sensitized Solar Cells. *Nano Energy* **2013**, *2*, 545–552. [CrossRef]

59. Ou, Y.; Lin, J.-D.; Zou, H.-M.; Liao, D.-W. Effects of Surface Modification of TiO_2 with Ascorbic Acid on Photocatalytic Decolorization of an Azo Dye Reactions and Mechanisms. *J. Mol. Catal. Chem.* **2005**, *241*, 59–64. [CrossRef]

60. Hoffmann, M.R.; Martin, S.T.; Choi, W.; Bahnemann, D.W. Environmental Applications of Semiconductor Photocatalysis. *Chem. Rev.* **1995**, *95*, 69–96. [CrossRef]

61. Konstantinou, I.K.; Albanis, T.A. TiO_2-Assisted Photocatalytic Degradation of Azo Dyes in Aqueous Solution: Kinetic and Mechanistic Investigations. *Appl. Catal. B Environ.* **2004**, *49*, 1–14. [CrossRef]

62. Bartolomei, B.; Bogo, A.; Amato, F.; Ragazzon, G.; Prato, M. Nuclear Magnetic Resonance Reveals Molecular Species in Carbon Nanodot Samples Disclosing Flaws. *Angew. Chem. Int. Ed.* **2022**, *61*, e202200038. [CrossRef]

63. Fan, Y.; Tao, T.; Wang, H.; Liu, Z.; Huang, W.; Cao, H. A Schiff Base-Functionalized Graphene Quantum Dot Nanocomposite for Preferable Picric Acid Sensing. *Dyes Pigment.* **2021**, *191*, 109355. [CrossRef]

64. Tang, J.; Hua, J.; Wu, W.; Li, J.; Jin, Z.; Long, Y.; Tian, H. New Starburst Sensitizer with Carbazole Antennas for Efficient and Stable Dye-Sensitized Solar Cells. *Energy Environ. Sci.* **2010**, *3*, 1736–1745. [CrossRef]

65. Saraswati, T.E.; Astuti, A.R.; Rismana, N. Quantitative Analysis by UV-Vis Absorption Spectroscopy of Amino Groups Attached to the Surface of Carbon-Based Nanoparticles. *IOP Conf. Ser. Mater. Sci. Eng.* **2018**, *333*, 012027. [CrossRef]

66. Xin, W.; Zhu, D.; Liu, G.; Hua, Y.; Zhou, W. Synthesis and Characterization of Mn–C–Codoped TiO_2 Nanoparticles and Photocatalytic Degradation of Methyl Orange Dye under Sunlight Irradiation. *Int. J. Photoenergy* **2012**, *2012*, 767905. [CrossRef]

67. Nečas, D.; Klapetek, P. Gwyddion: An Open-Source Software for SPM Data Analysis. 2012. Available online: http://gwyddion.net/ (accessed on 24 December 2024).

68. Sacco, A.; Matteoli, E. Isotopic Substitution Effects on the Volumetric and Viscosimetric Properties of Water-Dimethylsulfoxide Mixtures at 25 °C. *J. Solut. Chem.* **1997**, *26*, 527–535. [CrossRef]

69. Levitus, M. Tutorial: Measurement of Fluorescence Spectra and Determination of Relative Fluorescence Quantum Yields of Transparent Samples. *Methods Appl. Fluoresc.* **2020**, *8*, 033001. [CrossRef]

70. Luther, R.; Nikolopulos, A. Über die Beziehungen zwischen den Absorptionsspektren und der Konstitution der komplexen Kobaltamminsalze. *Z. Für Phys. Chem.* **1913**, *82U*, 361–384. [CrossRef]

71. Bligaard, T.; Bullock, R.M.; Campbell, C.T.; Chen, J.G.; Gates, B.C.; Gorte, R.J.; Jones, C.W.; Jones, W.D.; Kitchin, J.R.; Scott, S.L. Toward Benchmarking in Catalysis Science: Best Practices, Challenges, and Opportunities. *ACS Catal.* **2016**, *6*, 2590–2602. [CrossRef]